Equilibrium and Fractional Crystallization Experiments at 0·7 GPa; the Effect of Pressure on Phase Relations and Liquid Compositions of Tholeiitic Magmas

SAMUEL VILLIGER[1], PETER ULMER[1]* AND OTHMAR MÜNTENER[2]

[1]DEPARTMENT OF EARTH SCIENCES, ETH ZÜRICH, SONNEGGSTRASSE 5, CH-8092 ZÜRICH, SWITZERLAND

[2]INSTITUTE OF GEOLOGICAL SCIENCES, UNIVERSITY OF BERN, BALTZERSTRASSE 1, CH-3012 BERN, SWITZERLAND

Two series of anhydrous experiments have been performed in an end-loaded piston cylinder apparatus on a primitive, mantle-derived tholeiitic basalt at 0·7 GPa pressure and temperatures in the range 1060–1270°C. The first series are equilibrium crystallization experiments on a single basaltic bulk composition; the second series are fractionation experiments where near-perfect fractional crystallization was approached in a stepwise manner using 30°C temperature increments and starting compositions corresponding to that of the previous, higher temperature glass. At 0·7 GPa liquidus temperatures are lowered and the stability of olivine and plagioclase is enhanced with respect to clinopyroxene compared with phase equilibria of the same composition at 1·0 GPa. The residual solid assemblages of fractional crystallization experiments at 0·7 GPa evolve from dunites, followed by wehrlites, gabbronorites, and gabbros, to diorites and ilmenite-bearing diorites. In equilibrium crystallization experiments at 0·7 GPa dunites are followed by plagioclase-bearing websterites and gabbronorites. In contrast to low-pressure fractionation of tholeiitic liquids (1 bar–0·5 GPa), where early plagioclase saturation leads to the production of troctolites followed by (olivine) gabbros at an early stage of differentiation, pyroxene still crystallizes before or with plagioclase at 0·7 GPa. The liquids formed by fractional crystallization at 0·7 GPa evolve through limited silica increase with rather strong iron enrichment following the typical tholeiitic differentiation path from basalts to ferro-basalts. Silica enrichment and a decrease in absolute iron and titanium concentrations are observed in the last fractionation step after ilmenite starts to crystallize, resulting in the production of an andesitic liquid. Liquids generated by equilibrium crystallization experiments at 0·7 GPa evolve through constant SiO_2 increase and only limited FeO enrichment as a consequence of spinel crystallization and closed-system behaviour. Empirical calculations of the (dry) liquid densities along the liquid lines of descent at 0·7 and 1·0 GPa reveal that only differentiation at the base of the crust (1·0 GPa) results in liquids that can ascend through the crust and that will ultimately form granitoid plutonic and/or dacitic to rhyodacitic sub-volcanic to volcanic complexes; at 0·7 GPa the liquid density increases with increasing differentiation as a result of pronounced Fe enrichment, rendering it rather unlikely that such differentiated melt will reach shallow crustal levels.

INTRODUCTION

Numerous processes have been identified that modify the compositions of mantle-derived basaltic magmas at different depths during their ascent from the source region towards the surface. In addition to assimilation of country rocks, trapping of interstitial liquids in cumulates, mixing of different magma types and replenishment of magma chambers with less differentiated magmas, crystal fractionation is generally identified as the predominant process operating in crustal magma reservoirs.

Petrological, geochemical (including isotope geochemistry) and experimental studies on continental and oceanic flood basalts (Cox, 1980; Thompson *et al.*, 1980;

*Corresponding author. Telephone: +41-1-632-3955. Fax: +41-1-632-1088. E-mail: peter.ulmer@erdw.ethz.ch

Lightfoot *et al.*, 1990) clearly support the view that crystal fractionation is the predominant process involved in the evolution of continental basalts once they cross the crust–mantle boundary. Underplating of large volumes of mafic magma at the base of the thinned continental crust during rifting is suggested by geophysical studies of rifted continental margins (Mutter *et al.*, 1984; Holbrook & Kelemen, 1993). Exposed sections of lower crustal rocks in the Alps such as the Malenco (Müntener *et al.*, 2000; Hermann *et al.*, 2001) or the Ivrea–Verbano Zone (Rivalenti *et al.*, 1975, 1984) reveal the presence of massive amounts of ultramafic to mafic cumulates of tholeiitic affinity. These cumulate rocks have been explained by igneous underplating at the crust–mantle boundary (e.g. Bergantz, 1989) and intrusion of the continental crust by basaltic magmas equilibrated at depths between 15 and 30 km (0·5–0·9 GPa; Demarchi *et al.*, 1998). These magmas are also thought to be responsible for the occurrence of widespread silicic magmatism that is temporally and spatially associated with the mafic intrusive rocks either as direct products of the crystallization of these magmas and/or by partial fusion of lower crustal lithologies by the heat provided by these magmas.

Experimental determinations of the olivine–cpx–plagioclase saturation surfaces of anhydrous basalts by Grove and coworkers (Tormey *et al.*, 1987; Bartels *et al.*, 1991; Grove *et al.*, 1992; Kinzler & Grove, 1992; Yang *et al.*, 1996) led to quantitative models over a range of pressures, temperatures and compositions. Estimated crystallization pressures on the basis of cpx-saturated liquids from a large dataset of mid-ocean ridge glasses (Michael & Cornell, 1998; Herzberg, 2004; Villiger *et al.*, 2006) show that mid-ocean ridge basalts crystallize at variable depths beneath spreading centres, both in the oceanic crust and within the underlying mantle, at depths to 30 km. The highest crystallization pressures are obtained for basaltic glasses extruded at ultra-slow spreading ridges, particularly along fracture zones.

The majority of experiments on anhydrous basaltic liquids at elevated pressures (Bender *et al.*, 1978; Baker & Eggler, 1983, 1987; Grove & Bryan, 1983; Elthon & Scarfe, 1984; Gust & Perfit, 1987; Grove *et al.*, 1990, 1992; Bartels *et al.*, 1991; Fram & Longhi, 1992; Kinzler & Grove, 1992) have been designed to establish near-liquidus phase relations (multiple-saturation experiments). These experiments generally do not cover the entire temperature and composition range of magmatic differentiation. In addition, some of these studies were performed with starting compositions that are not consistent with a primary mantle origin, i.e. using bulk compositions with Mg-number [molar $Mg/(Mg + Fe_{tot})$] considerably below 0·70, values inconsistent with equilibration with mantle peridotite (Roedder & Emslie, 1970; Ulmer, 1989).

Cumulate rocks with textures varying from adcumulates to orthocumulates are the product of solid–liquid separation processes, most obviously demonstrated by cumulate rocks exhibiting modal and grain-size layering. They imply fractional crystallization in a dynamic magma system as the predominant differentiation process. Applying equilibrium crystallization or partial melting experiments performed on a constant bulk composition cannot simulate this process accurately. The experimental liquid lines of descent result in different phase relations and liquid compositions for fractional crystallization and for equilibrium crystallization experiments in a natural multi-component system at 1·0 GPa (Villiger *et al.*, 2004). Attempts to reproduce experimental liquid lines of descent with currently available thermodynamic models (e.g. MELTS and pMELTS, Ghiorso & Sack, 1995; Asimow & Ghiorso, 1998; Ghiorso *et al.*, 2002) result in liquid compositions and phase relations that are significantly different from our previous experimental results at 1·0 GPa (Villiger *et al.*, 2004).

In summary, field, petrological and geochemical studies on crustal rocks of tholeiitic affinity unambiguously underline the importance of crystal–liquid differentiation processes operating at pressures corresponding to conditions at the base of the continental crust or within the mantle below mid-ocean ridges.

To explore the effects of pressure on the two crystallization processes, we performed two series of piston cylinder experiments at 0·7 GPa: fractional and equilibrium crystallization. We present quantitative data on the phase relations, phase proportions, the compositions of melts and coexisting crystalline products as well as mineral–liquid partitioning, derived from both fractional and equilibrium crystallization experiments. To resolve the effect of crystallization pressure on the differentiation of tholeiitic magmas, the data are compared with our previous fractional and equilibrium crystallization experiments at 1·0 GPa using the same starting materials (Villiger *et al.*, 2004) and equilibrium crystallization experiments conducted between 1 bar and 1·0 GPa on different natural starting compositions (Bender *et al.*, 1978; Baker & Eggler, 1983, 1987; Grove & Bryan, 1983; Elthon & Scarfe, 1984; Gust & Perfit, 1987; Tormey *et al.*, 1987; Grove *et al.*, 1990, 1992; Bartels *et al.*, 1991; Fram & Longhi, 1992; Kinzler & Grove, 1992; Yang *et al.*, 1996; Sano *et al.*, 2001; P. Ulmer, unpublished data). Calculated densities for the liquids in the fractional and equilibrium crystallization experiments and their consequences for ascent of primitive and differentiated magmas from lower crustal magma reservoirs are presented and discussed.

EXPERIMENTAL TECHNIQUES
Experimental strategy

Two contrasting experimental series were performed at 0·7 GPa, subsequently referred to as equilibrium and fractional crystallization experiments, respectively.

For the equilibrium crystallization experiments a single starting composition (a primitive tholeiitic basalt) was used. Temperature was lowered by 30°C for successive runs. An approximation to pure fractional crystallization was achieved by a stepwise approach. In each experiment the liquid compositions were determined. The succeeding experiment was then performed at a 30°C lower temperature starting with a synthetic mixture that corresponds to the liquid composition from the previous (higher temperature) experiment. This approach used to simulate fractional crystallization (by removal of all solid phases) has successfully been applied by Villiger *et al.* (2004) for anhydrous tholeiitic liquids at 1·0 GPa and for fractionation of a hydrous picrobasalt and a high-Mg basaltic andesite by Kägi (2000). This experimental strategy results in variable but relatively high melt fractions (from 0·94 to 0·40) that allow us to perform experiments over a large range of differentiation with the possibility of obtaining precise liquid compositions. Based on temperature reproducibility in piston cylinder experiments (±15°C), temperature increments of 30°C were chosen for successive experiments. Smooth variations of phase relations and liquid compositions are taken as an indication that we did not seriously overstep any important peritectic reaction that might significantly alter the overall liquid line of descent.

Starting materials

The starting compositions used for the anhydrous experiments at 0·7 GPa are listed in Table 1. Composition HK#19 represents a primitive basaltic glass composition (Mg-number 0·76) derived through dry partial melting experiments by Hirose & Kushiro (1993) on KLB1 peridotite composition. This composition is in equilibrium with a lherzolitic residue (ol, opx, cpx) at 1·5 GPa and 1350°C. To compare the experimental results at 0·7 GPa with the previous experiments at 1·0 GPa (Villiger *et al.*, 2004), the same initial starting composition was used. Equilibrium crystallization experiments were performed with composition HK#19.1 (HK#19 + 0·5 wt % pure anorthite seeds added to prevent overstepping of the plagioclase liquidus as a result of retarded nucleation); fractional crystallization experiments started with HK#19.2, which contained 0·5 wt% natural forsterite (Fo$_{90}$) in addition to anorthite used to guarantee olivine saturation at the liquidus at 1 GPa (Villiger *et al.*, 2004). Starting materials 7Fr1 to 7Fr7 correspond to the average glass compositions of the previous, higher temperature experiment (Tables 1 and 3) renormalized to 100% oxide total. Starting materials were synthesized from chemicals for each subsequent fractional crystallization experiment. The choice of slightly different initial starting compositions used for fractional and equilibrium crystallization experiments has been discussed by Villiger *et al.* (2004).

The starting materials consist of mixes of fired synthetic and natural oxides, silicates and carbonates. A mixture of finely ground refractory components (SiO$_2$, TiO$_2$, Al$_2$O$_3$, CaAl$_2$Si$_2$O$_8$, CaCO$_3$, MgO, Cr$_2$O$_3$) was fired for 2 h at 1100°C to completely dehydrate the oxides and decarbonize the CaCO$_3$. This mixture was added to the finely ground reactive components (Fe$_2$SiO$_4$, MnO,

Table 1: Starting compositions

Sample	SiO$_2$	TiO$_2$	Al$_2$O$_3$	Cr$_2$O$_3$	FeO$_{tot}$	MnO	MgO	CaO	Na$_2$O	K$_2$O	Mg-no.
HK#19	49·10	0·60	15·17	0·36	7·54	0·14	13·10	12·27	1·58	0·08	0·76
HK#19.1	49·07	0·60	15·28	0·36	7·50	0·14	13·04	12·31	1·57	0·08	0·76
HK#19.2	48·67	0·57	14·55	0·34	7·56	0·14	14·81	11·73	1·50	0·08	0·78
7Fr1	50·24	0·59	14·59	0·31	7·36*	0·16	12·85	12·17	1·65	0·09	0·76
7Fr2	51·55	0·61	14·99	0·19	7·35	0·13	10·78	12·32	1·96	0·14	0·72
7Fr3	52·01	0·74	16·22	0·05	8·11	0·14	8·05	11·91	2·55	0·22	0·64
7Fr4	52·25	0·95	15·95	0·02	9·90	0·16	7·22	10·32	2·92	0·31	0·57
7Fr5	53·38	1·79	14·99	0·02	12·53	0·20	4·38	8·43	3·52	0·75	0·38
7Fr6	53·88	2·58	13·82	0·02	14·62	0·23	2·94	7·00	3·65	1·26	0·26
7Fr7	54·25	3·10	12·74	0·03	16·65	0·21	1·80	5·91	3·40	1·91	0·16

The starting material HK#19 used in equilibrium crystallization experiments represents a basaltic liquid in equilibrium with a lherzolitic residuum at 1·5 GPa and 1350°C (Hirose & Kushiro, 1993). HK#19.1 is HK#19 + 0·5 wt% pure anorthite seeds. For the fractional crystallization experiment SV76 HK#19.2 [HK#19 + 0·5 wt% anorthite seeds + 5·0 wt% natural forsterite (Fo$_{90}$)] was used. Starting materials 7Fr1 and 7Fr7 correspond to the glass compositions of the previous, 30°C higher temperature, experiment (see Tables 2 and 3). FeO$_{tot}$ and Mg-number: all Fe as Fe^{2+}. Uncertainties from weighing are <0·1% relative for the major elements and <1% relative for the minor elements (Cr$_2$O$_3$, MnO, K$_2$O).
*FeO$_{tot}$ was corrected for experiments with ΔFe >2·0 wt% (see Table 2).

Na_2SiO_3, $KAlSi_3O_8$,) in weight proportions appropriate to obtain 2·5 g of starting material. The final powders were homogenized by regrinding in an agate mill for 1/2 h under ethanol and dried for at least 1 day at 220°C.

Experimental set-up

To minimize Fe loss to the noble metal capsule and to constrain the fO_2 near the $C–CO_2–CO$ equilibrium, the Pt–graphite double capsule technique was applied (Ulmer & Luth, 1991). A graphite container was filled with the powdered starting material and closed with a tight-fitting lid (2·6 mm outer diameter; 1·5 mm inner diameter). The graphite container was placed in a 3·0 mm Pt-capsule and welded shut.

All nominally anhydrous experiments were performed in solid media high-pressure apparatus at the ETH Zürich. An end-loaded piston cylinder apparatus (Boyd & England, 1960) with a 14 mm bore was used. NaCl–Pyrex–MgO assemblies with a friction correction of -3% applied to the nominal pressure were used to the highest temperatures. Pressure was calibrated against the univariant reaction fayalite + quartz = orthoferrosilite at 1000°C and 1·41 GPa (Bohlen et al., 1980) and the quartz–coesite transition at 1000°C and 3·07 GPa (Bose & Ganguly, 1995). This experimental study was conducted in the lower pressure range feasible for piston cylinder apparatus and, therefore, pressure accuracy and reproducibility are important issues because we compare 0·7 GPa experiments (this study) with 1·0 GPa experiments reported by Villiger et al. (2004). The assembly employed [NaCl outer sleeve shielded by Pyrex glass from the graphite furnace and high-porosity ($>10\%$) MgO as internal parts] was tested for 'low' pressure performance by measuring the LiCl and CsCl melting curves that have accurately been determined by Clark (1959) as a function of pressure and temperature. We used a 'pressure analysis technique' to determine the melting point of LiCl in situ as described by Brey et al. (1990) for silver melting in a belt apparatus in the range 0·5–0·8 GPa. Absolute precision and accuracy were about 0·05 GPa. Temperatures were measured with $Pt_{94}Rh_6–Pt_{70}Rh_{30}$ (B-type) thermocouples with an estimated accuracy of ± 10°C, without taking into account the effect of pressure on the e.m.f. To assess potential 'thermocouple poisoning' of the Pt–Rh thermocouples we continuously monitored the output-power of the thyristor unit, which resulted in a nearly constant power demand over the duration of the experiment after an initial power increase attributed to thermal equilibration and mechanical relaxation of the assembly.

Analytical methods

All experimental run products were analysed using five spectrometer electron microprobes (Cameca SX50 and Jeol 8200) at the Institute for Mineralogy and Petrology,

ETH Zürich. A 15 kV accelerating potential, 7 nA beam current and 10 μm beam size were used for analyses of the quenched glasses. The crystalline phases were analysed with a 20 nA beam current and 1 μm beam size. All elements were analysed for 20 s, except for Na in quenched glasses, for which the counting time was 10 s to minimize potential Na loss. Depending on the quality of the polished surface of the experimental charges all glass analyses summed to between 96·4 and 99·6 wt % (Table 3). For graphic representation, calculation of modal proportions and internal consistency with previous experiments (Villiger et al., 2004), glass analyses have been normalized to 100 wt %. The same set of standards and identical data reduction schemes (ZAF) were used for both microprobes; results are, within statistical error, indistinguishable between the two electron probe microanalysers employed in this work.

Modal proportions of phases in the high-pressure run products reported in Table 2 were estimated using non-weighted least-squares regression analyses balancing the nominal composition of the bulk starting material against the averages of all analysed phases in the experimental charges. Errors indicated in Table 2 are the statistical errors calculated by the least-squares regression routine implemented in the EXCEL spreadsheet program. Table 2 reports the sum of the residuals squared (Σr^2), which is less than 0·36, except for SV76 (0·69). If calculated Fe loss (see Table 2 and discussion below) exceeded 2% relative, the least-squares regression was repeated omitting Fe from the calculation, which resulted in considerably smaller residuals without significant change of modal proportions. For experimental charges with spinel grains that were too small to be analysed by electron microprobe, spinel analyses from other experiments at similar conditions were used for the mass balance calculation (Table 2).

EXPERIMENTAL RESULTS

Conditions, phase assemblages and calculated proportions of experimental runs, as well as relative iron losses ($\triangle Fe\%$), are reported in Table 2. The compositions of quenched glasses and crystalline phases are listed in Table 3. Fe/Mg mineral–melt partition coefficients for olivine and pyroxenes, Al_2O_3, TiO_2 and Na_2O K_d values for pyroxenes, and $CaO/(Na_2O + K_2O)$ K_d values for plagioclase are listed in Table 4.

Iron loss

In most runs a limited amount of Fe was lost to the platinum capsule. Fe loss occurs through small cracks in the inner graphite capsule connecting the liquid with the outer Pt-capsule. In all runs relative Fe losses, estimated on the basis of mass balance calculations, were lower than 8·0%. In some runs (SV99, SV101, SV103, SV104) small amounts of Fe gain were calculated ($< -0·62\%$ relative),

Table 2: Experimental run conditions, phase assemblages and proportions

Run no.	Starting material	T (°C)	Time (h)	Run products	Phase proportions (wt %)	ΣR^2	ΔFe (%)
Equilibrium crystallization							
SV75	HK#19.1	1240	8·0	liq, ol, sp	95·7(7):3·2(6):1·0(5)	0·36	5·38
SV89	HK#19.1	1210	20·5	liq, cpx, opx, plg, sp	71·5(21):14·3(23):11·0(17):2·2(14):1·0(8)	0·03	4·14
SV90	HK#19.1	1180	72·5	liq, cpx, opx, plg, sp	45·8(15):38·6(8):3·8(6):4·4(10):7·4(2)	0·04	0·28
SV79	HK#19.1	1150	78·0	liq, cpx, opx, plg, sp	23·9(6):48·4(2):4·4(2):14·3(3):9·0(1)	0·00	0·07
Fractional crystallization							
SV76	HK#19.2	1270	5·0	liq, ol, sp	94·0(9):4·6(8):1·4(7)	0·69	8·00
SV96	7Fr1	1240	7·5	liq, ol, cpx, sp	88·0(10):3·3(4):6·8(11):1·9(2)	0·06	1·01
SV97	7Fr2	1210	20·0	liq, cpx, opx, plg, sp	69·9(11):15·6(6):6·6(5):6·7(7):1·1(1)	0·02	0·11
SV99	7Fr3	1180	46·2	liq, cpx, plg, sp	68·2(9):16·4(5):14·6(5):0·7(1)	0·03	−0·62
SV101	7Fr4	1150	114·2	liq, cpx, plg, sp	39·6(13):30·3(7):27·2(7):2·9(2)	0·06	−0·03
SV103	7Fr5	1120	162·0	liq, cpx, plg, sp	59·4(8):17·5(5):21·8(4):1·3(1)	0·02	0·04
SV104	7Fr6	1090	145·0	liq, cpx, plg, sp, ilm	64·9(40):13·6(20):20·2(23):0·6(4):0·7(5)	0·29	−0·22
SV107	7Fr7	1060	167·0	liq, cpx, plg, sp, ilm	52·9(28):20·0(13):21·6(18):1·7(3):3·7(3)	0·13	0·23

Starting materials 7Fr1 and 7Fr7 correspond to the glass compositions of the previous, 30°C higher temperature, experiment (see Tables 1 and 3). ΔFe is the difference between the FeO content of the bulk starting composition and the FeO in the bulk composition calculated by mass balance. Negative values indicate relative iron gain (relative weight per cent). Phase proportions are calculated by least-squares regressions. ΣR^2 indicates the quality of the regression. Numbers in parentheses represent the 2σ error from the regression analysis. Accordingly, 95·7(7) should be read as $95\cdot7\pm0\cdot7$.

which are statistically insignificant. Small iron losses or gains justify our assumption that a relatively constant bulk composition was maintained during the experiments.

Attainment of equilibrium

Figure 1 displays the Fe–Mg partitioning behaviour between the solid phases olivine, cpx, opx and the quenched liquids expressed as K_d values (all Fe as Fe^{2+}) plotted against temperature. They indicate a close approximation to equilibrium. The Fe/Mg olivine–liquid K_d is 0·31 for two fractional crystallization experiments, and 0·32 for one equilibrium crystallization experiment. These values are systematically lower than at 1·0 GPa (0·34–0·33, Villiger *et al.*, 2004). This is consistent with the K_d values calculated for basaltic compositions at 0·7 GPa (Ulmer, 1989) with an fO_2 constrained by the C–CO$_2$–CO equilibrium in this temperature range $(K_d = 0\cdot32)$. The pyroxene–liquid Fe–Mg K_d values in our experiments are in the same range as those reported from mantle partial melting experiments performed by Gaetani & Grove (1998). For coexisting pyroxenes, Fe–Mg K_d values for orthopyroxene (opx) tend to be lower than for clinopyroxene (cpx). Pyroxene–melt Fe–Mg K_d values in the equilibrium crystallization experiments decrease from 0·32 and 0·25 in a temperature interval from 1210°C and 1150°C whereas for the fractional crystallization experiments this trend is less obvious for cpx–melt K_d values (0·32–0·26) over the temperature interval 1240°C to

1060°C. Additionally, we observe a decrease of K_d with increasing differentiation consistent with increasing contents of Na$_2$O and K$_2$O and increasing degree of polymerization of coexisting liquids in equilibrium crystallization experiments as observed, for example, by Kushiro & Mysen (2002) for olivine–liquid Fe–Mg partitioning.

In most experimental charges pyroxenes and plagioclase exhibit some chemical zoning although, in general, the range of variation is small. In particular, the opx in run SV97 (1210°C, fractionation experiment) shows sector zoning with Al-poor $(2\cdot5\pm0\cdot3$ wt % Al$_2$O$_3$) and Al-rich sectors $(4\cdot5\pm0\cdot2$ wt % Al$_2$O$_3$). Plagioclase shows normal zoning with decreasing anorthite content from core to rim (e.g. SV97 plagioclase profile from core to rim: X_{An} 0·73–0·68). In these rare cases, average mineral compositions were used in the least-squares regression calculations to estimate the modal proportions of phases in the charges (see above). Anorthite-rich cores observed in some experiments originate from the pure anorthite seeds, indicating that chemical equilibrium was not always fully achieved. In such cases, rim compositions have been analysed. The regular behaviour of major and minor element partitioning between cpx and plg and the consistency of the liquid evolution with temperature (Table 4) indicates a close approximation to equilibrium. An additional indication for an overall successful approach to equilibrium is provided by the quality of mass balance calculations

Table 3: Electron microprobe analyses of run products in wt %

Run no.	Phase	n	SiO$_2$	TiO$_2$	Al$_2$O$_3$	Cr$_2$O$_3$	FeO$_{tot}$	MnO	MgO	CaO	Na$_2$O	K$_2$O	Total	Mg-no./X_{An}
Equilibrium crystallization														
SV75	melt	11	49·10(32)	0·58(2)	14·93(20)	0·29(2)	6·89(18)	0·20(3)	11·44(8)	12·60(12)	1·86(6)	0·08(1)	97·97(75)	0·75
	ol	16	40·67(5)	0·02(0)	0·06(0)	0·21(0)	9·59(2)	0·20(0)	49·64(9)	0·37(0)	<0·01	<0·01	100·77(12)	0·89
	sp	5	0·29(27)	0·24(1)	30·21(112)	38·79(105)	10·94(23)	0·07(14)	17·55(17)	0·33(4)	0·01(2)	<0·01	98·59(52)	0·74
SV89	melt	8	50·72(30)	0·72(6)	16·91(22)	0·10(3)	7·69(22)	0·21(8)	8·72(24)	12·26(19)	2·13(10)	0·11(2)	99·55(74)	0·67
	cpx	11	52·45(35)	0·25(2)	5·08(51)	1·02(10)	5·64(63)	0·22(4)	19·86(24)	16·53(53)	0·31(2)	<0·01	101·48(11)	0·86
	opx	13	53·82(22)	0·14(1)	4·95(26)	1·15(5)	7·38(23)	0·23(1)	29·68(27)	3·02(14)	0·07(2)	0·01(0)	100·47(52)	0·88
	plg	12	49·63(47)	0·03(1)	31·34(25)	0·01(1)	0·39(13)	0·02(1)	0·25(3)	15·86 (32)	3·02(6)	0·03(1)	100·61(26)	0·74
	sp*SV18	8	0·17(5)	0·15(1)	58·24(126)	9·15(134)	11·41(15)	0·31(4)	18·83(39)	0·18(2)	0·02(2)	<0·01	98·46(56)	0·75
SV90	melt	12	52·08(21)	1·14(3)	16·76(20)	0·06(1)	8·10(11)	0·17(3)	7·05(10)	10·53(7)	2·81(10)	0·17(1)	98·88(39)	0·61
	cpx	11	53·34(35)	0·37(5)	3·61(38)	0·51(6)	6·26(26)	0·21(5)	18·78(51)	17·50(47)	0·40(2)	0·01(1)	101·02(50)	0·84
	opx	10	55·29(43)	0·23(4)	3·62(48)	0·60(8)	9·22(14)	0·22(3)	29·63(35)	2·71(16)	0·06(1)	<0·01	101·59(24)	0·85
	plg	10	52·99(48)	0·05(1)	30·04(28)	0·01(1)	0·41(12)	0·01(1)	0·21(3)	13·53(31)	3·95(17)	0·05(1)	101·26(31)	0·65
	sp*SV21	7	0·13(4)	0·14(1)	63·21(170)	3·47(159)	13·77(19)	0·05(4)	19·48(28)	0·12(1)	0·02(2)	<0·01	100·55(28)	0·72
SV79	melt	10	54·74(21)	1·47(5)	14·86(8)	0·04(2)	7·99(6)	0·16(3)	4·70(13)	9·06(7)	3·07(8)	0·31(2)	96·40(34)	0·51
	cpx	12	52·81(33)	0·46(7)	2·51(19)	0·57(11)	7·72(48)	0·19(2)	18·44(50)	16·68(96)	0·35(3)	0·01(1)	99·80(33)	0·81
	opx	16	54·03(32)	0·30(2)	2·44(20)	0·42(3)	11·94(62)	0·23(2)	29·08(18)	2·64(11)	0·05(1)	0·01(0)	101·45(52)	0·81
	plg	9	52·02(29)	0·07(1)	29·78(56)	0·02(1)	0·40(4)	0·02(0)	0·15(2)	12·76(48)	4·27(21)	0·05(1)	99·57(57)	0·62
	sp	4	0·46(29)	0·12(2)	67·23(78)	0·12(13)	14·10(73)	0·10(4)	18·34(35)	0·24(10)	0·02(2)	0·01(1)	97·37(14)	0·70
Fractional crystallization														
SV76	liq	10	49·28(19)	0·58(1)	14·31(11)	0·31(3)	6·65(7)	0·15(3)	12·60(14)	11·94(5)	1·61(5)	0·09(1)	97·52(46)	0·76
=7Fr1	ol	16	41·14(35)	0·01(1)	0·05(1)	0·19(2)	8·79(6)	0·14(2)	50·15(38)	0·27(4)	<0·01	0·01(0)	100·75(49)	0·91
	sp	3	0·04(1)	0·26(1)	28·96(54)	38·67(44)	11·01(17)	0·21(0)	20·13(13)	0·22(1)	0·02(0)	0·01(0)	99·53(6)	0·77
SV96	liq	10	51·03(22)	0·60(4)	14·84(16)	0·19(2)	7·28(7)	0·13(2)	10·67(7)	12·19(8)	1·94(6)	0·14(2)	99·01(40)	0·72
=7Fr2	ol	9	40·97(5)	0·01(1)	0·05(0)	0·15(1)	10·41(8)	0·14(1)	49·19(18)	0·37(2)	0·01(1)	<0·01	101·30(29)	0·89
	cpx	11	52·32(47)	0·26(9)	4·24(53)	1·25(15)	4·01(45)	0·11(1)	19·98(41)	18·11(54)	0·31(3)	<0·01	100·60(25)	0·90
	sp	6	0·34(21)	0·18(2)	41·51(51)	26·73(61)	11·02(9)	0·14(2)	19·44(21)	0·34(3)	0·01(1)	<0·01	99·95(42)	0·78

Sample	phase	n												
SV97	liq	18	51·16(19)	0·73(3)	15·95(20)	0·05(2)	7·98(14)	0·14(3)	7·92(10)	11·71(9)	2·51(10)	0·21(2)	98·37(54)	0·64
=7Fr3	cpx	14	51·92(29)	0·28(3)	4·30(38)	0·49(11)	5·98(53)	0·17(2)	18·86(25)	17·78(32)	0·37(3)	0·01(1)	100·15(21)	0·85
	opx	18	54·35(50)	0·14(2)	3·92(57)	0·50(7)	8·48(52)	0·17(2)	29·65(30)	2·65(16)	0·04(1)	0·01(0)	99·91(21)	0·86
	plg	23	50·39(47)	0·04(1)	28·62(82)	0·02(2)	0·40(6)	0·01(1)	0·37(8)	15·27(23)	3·46(13)	0·06(1)	98·65(116)	0·71
	sp	5	0·09(2)	0·12(2)	65·87(17)	0·01(1)	12·96(21)	0·15(4)	19·65(15)	0·14(1)	<0·01	0·01(1)	99·01(24)	0·73
SV99	liq	13	51·80(27)	0·95(3)	15·77(11)	0·02(2)	9·82(14)	0·16(3)	7·20(12)	10·22(7)	2·88(13)	0·31(3)	99·14(41)	0·57
=7Fr4	cpx	15	52·64(28)	0·42(4)	3·59(29)	0·13(2)	7·61(60)	0·19(2)	17·72(31)	18·52(74)	0·38(5)	0·01(1)	101·20(40)	0·81
	plg	34	52·82(69)	0·05(2)	29·28(48)	0·01(1)	0·47(8)	0·02(1)	0·25(6)	13·39(37)	4·31(20)	0·09(1)	100·69(74)	0·63
	sp	3	0·08(3)	0·23(2)	66·70(38)	0·03(1)	13·51(14)	0·11(1)	19·13(17)	0·15(1)	<0·01	<0·01	99·91(35)	0·72
SV101	liq	11	52·63(36)	1·77(6)	14·78(14)	0·02(1)	12·35(15)	0·19(3)	4·32(7)	8·22(6)	3·47(10)	0·74(3)	98·50(45)	0·38
=7Fr5	cpx	12	51·73(28)	0·73(8)	2·50(31)	0·09(2)	13·90(62)	0·36(3)	16·62(38)	14·34(81)	0·37(4)	0·01(1)	100·64(31)	0·68
	plg	10	56·65(31)	0·08(1)	27·07(26)	0·02(1)	0·50(15)	0·04(2)	0·13(4)	10·27(24)	5·85(9)	0·27(1)	100·87(42)	0·49
	sp	4	0·31(13)	0·48(19)	63·44(36)	<0·1	21·43(60)	0·18(2)	14·69(29)	0·17(4)	0·02(1)	<0·01	100·71(41)	0·55
SV103	liq	10	53·13(24)	2·54(5)	13·63(12)	0·02(2)	14·42(9)	0·22(3)	2·90(5)	6·91(4)	3·60(8)	1·25(2)	98·61(41)	0·26
=7Fr6	cpx	22	50·78(21)	0·89(7)	2·13(19)	0·09(1)	19·19(108)	0·42(3)	14·50(51)	12·88(148)	0·30(4)	0·01(1)	101·20(37)	0·57
	plg	15	58·50(51)	0·11(1)	26·25(30)	0·01(1)	0·71(26)	0·02(1)	0·08(3)	8·99(26)	6·38(12)	0·48(3)	101·54(36)	0·44
	sp*SV61	9	0·15(7)	0·69(9)	60·64(30)	0·02(1)	29·45(24)	0·18(1)	9·20(12)	0·11(2)	0·01(2)	<0·01	100·44(32)	0·36
SV104	liq	10	53·28(30)	3·04(5)	12·52(8)	0·03(2)	16·35(19)	0·21(3)	1·77(6)	5·98(6)	3·34(5)	1·88(5)	98·39(27)	0·16
=7Fr7	cpx	10	48·54(26)	1·02(6)	1·79(13)	0·04(2)	23·62(80)	0·46(3)	9·90(29)	13·90(82)	0·30(2)	0·02(1)	99·58(47)	0·43
	plg	15	59·47(67)	0·13(3)	24·46(53)	0·01(1)	0·75(22)	0·01(1)	0·06(3)	7·39(54)	6·78(18)	1·05(12)	100·11(39)	0·38
	sp*SV63	8	0·13(7)	0·76(12)	59·42(39)	0·01(1)	31·81(26)	0·26(2)	5·82(16)	0·09(2)	0·02(1)	0·01(1)	98·32(47)	0·25
	ilm	6	0·12(3)	51·44(17)	0·29(2)	0·08(2)	42·61(29)	0·44(3)	1·92(4)	0·38(4)	0·03(3)	0·02(0)	97·33(36)	0·07
SV107	liq	24	56·77(40)	1·82(6)	11·61(8)	0·01(1)	15·01(22)	0·24(2)	0·69(2)	4·32(5)	3·13(5)	3·11(7)	96·71(29)	0·08
	cpx	10	48·78(26)	0·93(5)	1·59(9)	0·03(2)	29·48(109)	0·45(6)	5·67(21)	12·71(104)	0·28(3)	0·05(3)	99·97(25)	0·26
	plg	12	61·07(38)	0·10(3)	23·05(22)	0·01(1)	0·85(6)	0·01(1)	<0·01	6·04(28)	6·51(7)	1·88(13)	99·51(27)	0·33
	sp*SV63	8	0·13(7)	0·76(12)	59·42(39)	0·01(1)	31·81(26)	0·26(2)	5·82(16)	0·09(2)	0·02(1)	0·01(1)	98·32(47)	0·25
	ilm	7	0·48(2)	50·50(25)	0·36(2)	0·08(3)	45·91(26)	0·31(1)	1·02(8)	0·29(2)	0·04(2)	0·06(0)	99·01(36)	0·04

FeO_{tot} and Mg-number: all Fe as Fe^{2+}. Numbers in parentheses indicate standard errors (2σ) from average analysis. Accordingly, 49·10(32) should be read as 49·10 ± 0·32. Glass compositions referring to starting materials 7Fr1–7Fr7 are given in the column for run number. *n*, number of analyses. sp* indicates spinel analysis taken from other experimental runs for mass balance because in these runs spinels were too small to be analysed successfully (SV61, SV62: Villiger *et al.*, 2004; SV18, SV21: unpublished data).

Table 4: Distribution coefficients (K_d) between crystals and liquid of anhydrous experiments at 0·7 GPa

Run no.	K_d(Fe/Mg)			K_d(Al)		K_d(Ti)	K_d(Na)	K_d[Ca/(Na + K)]
	ol	cpx	opx	cpx	opx	cpx	cpx	plg
Equilibrium crystallization								
SV75	0·32							
SV89		0·32	0·28	0·30	0·29	0·35	0·15	0·95
SV90		0·29	0·27	0·21	0·21	0·32	0·14	0·96
SV79		0·25	0·24	0·16	0·16	0·30	0·11	1·10
Fractional crystallization								
SV76	0·31							
SV96	0·31	0·29		0·28		0·43	0·16	
SV97		0·32	0·28	0·27	0·24	0·38	0·14	1·01
SV99		0·31		0·23		0·44	0·13	0·95
SV101		0·29		0·17		0·41	0·10	0·85
SV103		0·27		0·15		0·34	0·08	0·92
SV104		0·26		0·14		0·33	0·09	0·85
SV107		0·27		0·13		0·51	0·09	1·05

K_d(Fe/Mg) calculated as $FeO_{xtal}*MgO_{liq}/FeO_{liq}*MgO_{xtal}$; K_d(Al) calculated as $Al_2O_{3xtal}/Al_2O_{3liq}$; K_d(Ti) as TiO_{2xtal}/TiO_{2liq}; K_d(Na) as Na_2O_{xtal}/Na_2O_{liq}; K_d[Ca/(Na + K)] calculated as $[CaO_{plg}/(Na_2O_{plg} + K_2O_{plg})]/[CaO_{liq}/(Na_2O_{liq} + K_2O_{liq})]$.

performed with the average analyses of solid and quenched liquid phases listed in Table 2.

Estimate of oxygen fugacity

The oxygen fugacity of the piston cylinder experiments performed at 0·7 GPa and 1300–1060°C was calculated with the empirical equations of Ulmer & Luth (1991) and Frost & Wood (1995), resulting in log fO_2 values of −8·8 to −11·2 with decreasing temperature. These values apply only if the hydrogen fugacity in our system is minimal and, therefore, the graphite stability reaches its maximum in the C–COH system. To minimize the fH_2 in our experiments we used MgO spacers around, below and above the capsule. Such assemblies provide very oxidizing conditions [several log units above the Ni–NiO (NNO) equilibrium] and hence impose a rather low intrinsic hydrogen fugacity, as verified by Kägi (2000) for identical assemblies at 1·0 GPa pressure. In addition, this approach minimizes the production of H_2O by hydrogen diffusion from the surrounding assembly material and provides a close approach to truly anhydrous (water-free) experiments. Small amounts of CO_2 produced by oxidation of the graphite sample container cannot be completely excluded. The calculated oxygen fugacities of the quenched liquids in equilibrium with graphite are 2·1–1·7 log units below the quartz–fayalite–magnetite

(QFM) equilibrium. Fe^{3+}/Fe^{2+} ratios calculated with the equation of Kress & Carmichael (1991) vary between 0·032 and 0·026. Consequently, the molar Mg-number is calculated assuming all Fe as Fe^{2+}. This varies between 0·75 and 0·51 in glasses obtained in the equilibrium crystallization experiments and from 0·76 to 0·09 in glasses produced in the fractional crystallization experiments.

The fO_2 of both equilibrium and fractional crystallization experiments is buffered along the C–CO–CO_2 equilibrium and, therefore, our experimental system represents an open system with respect to oxygen. Natural systems are often regarded as closed systems where the Fe^{3+}/Fe^{2+} ratios of the crystallizing assemblage exert the dominant control on oxygen fugacity (e.g. Muan, 1958). However, our experiments were purposely run at low fO_2 to keep the Fe^{3+}/Fe^{2+} very low. Consequently, the open-system behaviour with respect to oxygen that is intrinsic to our experimental setup should not dramatically affect the liquid line of descent as inferred for more oxidizing systems (at fO_2 corresponding to FMQ) by Ghiorso & Carmichael (1985).

Crystallization sequence at 0·7 GPa

The crystallization sequence for equilibrium crystallization experiments in the temperature interval between 1240°C and 1150°C starts with olivine (ol) and Cr-rich spinel (sp) as liquidus phases. Ol disappears from the crystallizing assemblage at 1210°C, when cpx, plagioclase (plg) and opx form the crystallizing phase assemblage. Between 1210°C and 1150°C cpx, opx, plg and sp are the stable phases.

In the fractional crystallization series ol and sp are the liquidus phases at 1270°C. Unlike the equilibrium crystallization experiments, the solid phases at 1240°C are ol, cpx and sp. In this series, the disappearance of olivine and the first occurrence of plg are located at 1210°C co-precipitating with cpx, opx and sp. Between 1180°C and 1120°C cpx, plg and sp crystallized. At 1090°C and 1060°C ilmenite (ilm) is stable together with cpx, plg and sp.

Calculated fractions of liquid and solid phases at 0·7 GPa

The calculated melt fractions decrease from 95·7 to 23·9 wt % in equilibrium crystallization experiments between 1240°C and 1150°C. Melt fractions in fractional crystallization experiments vary between 94·0 and 39·6 wt % in single fractionation steps. For these experiments it is more useful to use cumulative melt fractions, which represent the amount of liquid left relative to the initial starting composition (HK#19.2). These are plotted against temperature in Fig. 2 and range from 94·0 to 3·2 wt %. Melt fractions calculated independently assuming K_2O behaves as a completely incompatible oxide component are identical
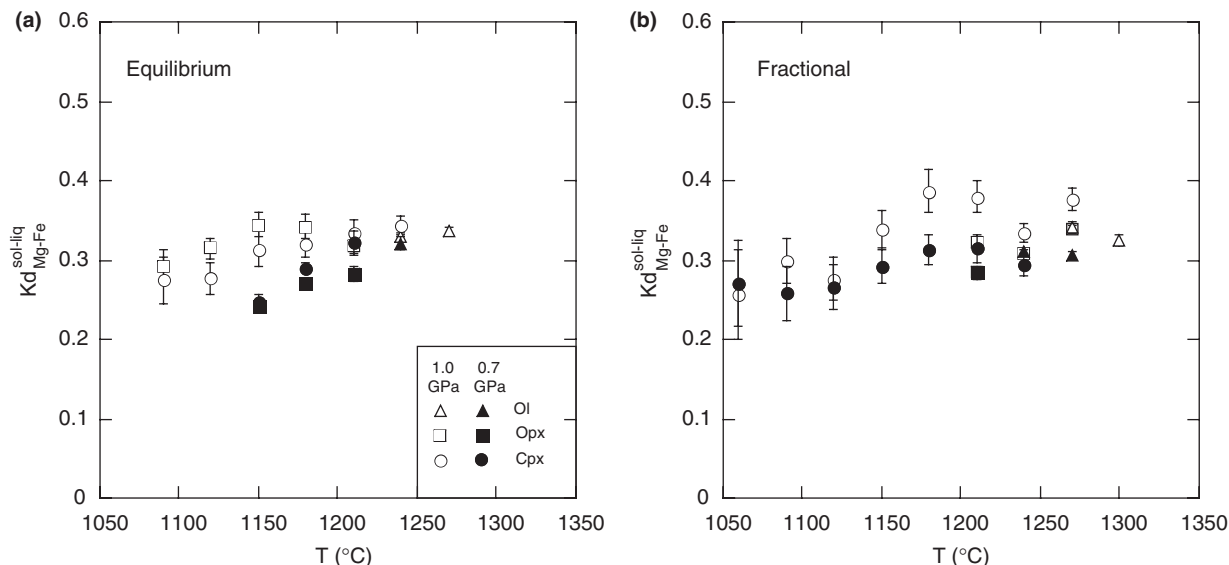
Fig. 1. Fe–Mg partitioning [$K_d = (Fe/Mg)_{solid}/(Fe/Mg)_{liquid}$] between crystals and melt as a function of temperature (°C): (a) equilibrium crystallization at 0·7 GPa (this study) and 1·0 GPa (Villiger *et al.*, 2004); (b) fractional crystallization at 0·7 GPa (this study) and 1·0 GPa (Villiger *et al.*, 2004). Error bars indicate 2σ standard errors.
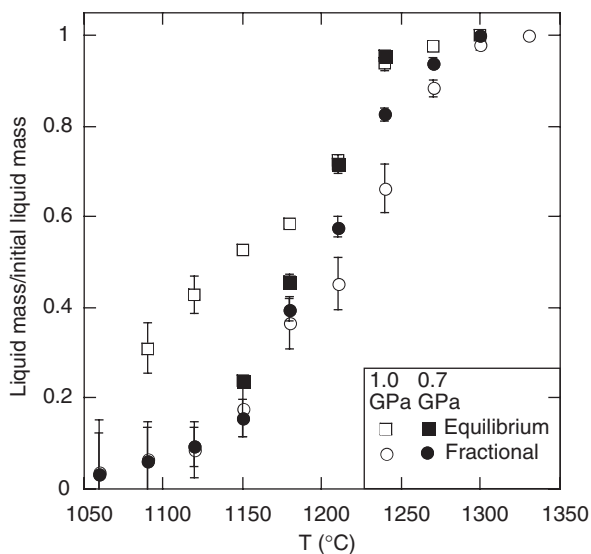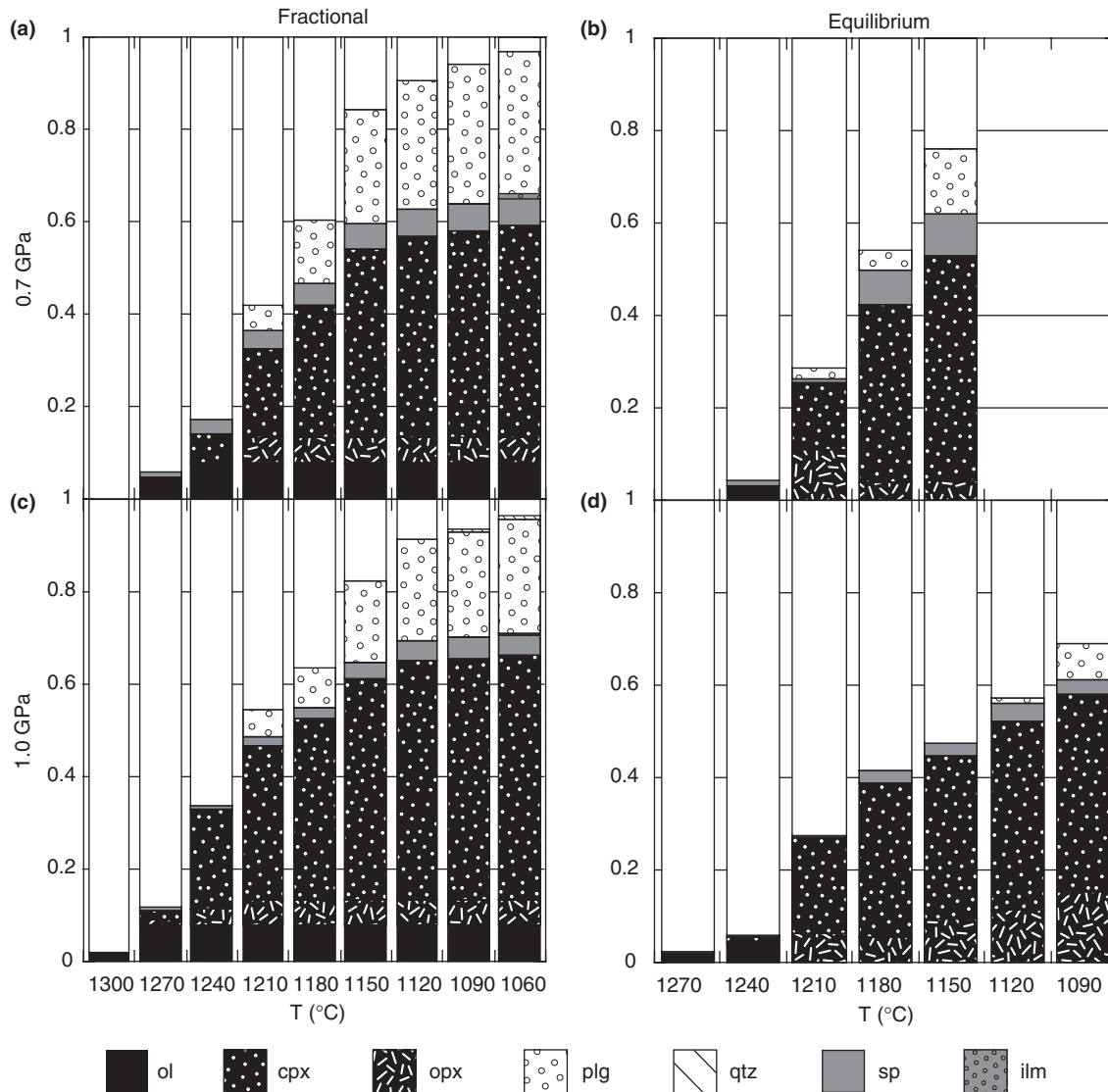

Fig. 2. Liquid mass/initial liquid mass vs temperature (°C) for equilibrium and fractional crystallization experiments at 0·7 and 1·0 GPa. For fractionation experiments the cumulative melt fractions (product of melt fraction in each fractionation step) are plotted. Error bars indicate 2σ standard errors calculated from the least-squares regression analysis (Table 2). Data for equilibrium and fractional crystallization experiments at 1·0 GPa are taken from Villiger *et al.* (2004).

within error for equilibrium crystallization experiments at 0·7 GPa and for both experimental series at 1·0 GPa (Villiger *et al.*, 2004). They are less accurate for fractional crystallization experiments at 0·7 GPa because higher fractions of K_2O are dissolved in plagioclase as an orthoclase

component (see discussion of plagioclase compositions). The slopes of the trends in Fig. 2 define the crystallization rates per degree Celsius. The crystallization rates for both equilibrium and fractional processes at 0·7 GPa increase with the onset of plagioclase precipitation, similar to calculated liquid mass/initial liquid mass at 200 MPa (Kelemen & Aharonov, 1998), whereas at 1·0 GPa an increase of the crystallization rate is observed with the crystallization of orthopyroxene (Villiger *et al.*, 2004).

Figure 3 displays stack diagrams of calculated fractions of liquid and solid phases from fractional (Fig. 3a) and equilibrium crystallization (Fig. 3b) experiments at 0·7 GPa. Melt and solid fractions of fractional (Fig. 3c) and equilibrium crystallization experiments (Fig. 3d) at 1·0 GPa are given for comparison. For fractional crystallization experiments cumulative solid masses have been calculated and are shown in Fig. 3. Every single phase of each fractionation step is multiplied by the accumulated liquid mass and added to the masses of the previous fractionation step.

At 0·7 GPa near-perfect fractional crystallization was simulated in seven steps between 1270°C and 1060°C, resulting in the crystallization of 96·8 wt % of solid phases with respect to the initial mass of liquid (HK#19.2). At 1060°C the accumulated solids are composed of 7·7 wt % ol, 5·5 wt % opx, 46 wt % cpx, 31·1 wt % plg, 6·0 wt % sp and 0·3 wt % ilm. At 1·0 GPa near-perfect fractional crystallization of the same starting composition in nine steps between 1300°C and 1060°C resulted in 96·3 wt % of solid phases

Fig. 3. Bar diagrams displaying melt and solid fractions at each experimental temperature for: (a) fractional crystallization experiments at 0·7 GPa; (b) equilibrium crystallization experiments at 0·7 GPa; (c) fractional crystallization experiments at 1·0 GPa; (d) equilibrium crystallization experiments at 1·0 GPa. Experimental data at 1·0 GPa are taken from Villiger *et al.* (2004). For fractionation experiments the cumulative melt = product of melt fraction in each fractionation step and the solid fractions = product of solid fractions and the cumulative melt fraction added to the solid fractions of the previous fractionation step.

(Villiger *et al.*, 2004). Compared with the new experimental series at 0·7 GPa the total accumulated solids at 1 GPa contain comparable amounts of ol (7·7 wt %) and opx (5·4 wt %), higher amounts of cpx (53 wt %), lower amounts of plg (24·8 wt %), sp (4·6 wt %) and ilm (0·2 wt %), and, in addition, 0·5 wt % qtz.

The solid assemblages of the equilibrium crystallization experiments at 0·7 GPa contain larger amounts of plg and sp than at 1·0 GPa. Despite the positive Clapeyron slope of the liquidus, earlier crystallization of plg at 0·7 GPa (1210°C) compared with the equilibrium

crystallization experiments at 1·0 GPa (1120°C) leads to more efficient crystallization at a given (sub-liquidus) temperature, which is clearly evident from comparison of Fig. 3b and Fig. 3d.

Liquid lines of descent

The anhydrous liquid lines of descent at 0·7 GPa are shown in the ol–cpx–qtz projection in Fig. 4: quenched glass compositions have been recalculated into mineral end-member components according to the method of Grove *et al.* (1992) and are projected onto the ol–cpx–qtz
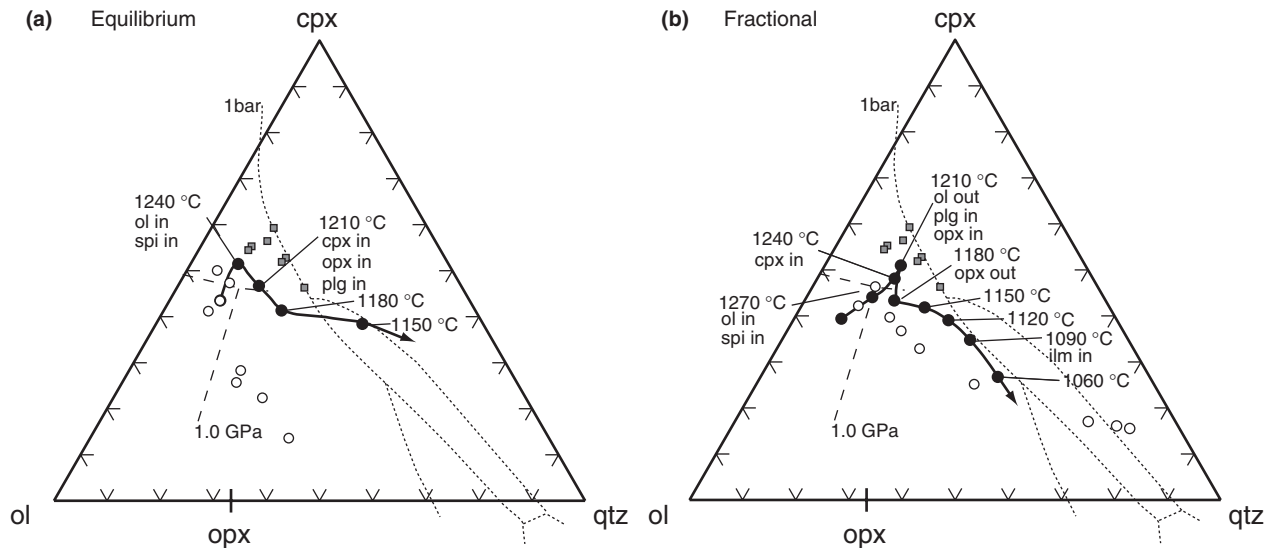
Fig. 4. Normative pseudo-ternary cpx–olivine–quartz diagram, illustrating the liquid lines of descent (glass compositions) for (a) anhydrous equilibrium and (b) fractional crystallization experiments. Experimental data at 0·7 GPa (filled symbols) and at 1·0 GPa (open symbols; Villiger et al., 2004) are plotted. Data at 1 bar are taken from Yang et al. (1996). The 1 bar (dotted lines) and 1·0 GPa (dashed lines) phase boundaries are from Grove & Baker (1984). Normalization into six components in oxygen units (ol, cpx, plg, qtz, orthoclase, oxide) is after Grove *et al.* (1992); compositions are projected from plagioclase, orthoclase and oxide. Temperatures and phase appearance (in) or disappearance (out) are noted along the liquid lines of descent for each projected 0·7 GPa melt composition.

plane of the basalt tetrahedron from a normative oxide phase and feldspar. The liquids of equilibrium and fractional crystallization at 0·7 GPa evolve from olivine-normative to quartz-normative compositions. They follow similar trends with decreasing temperature, but the liquids of the equilibrium crystallization experiments evolve towards more cpx-rich compositions, as a result of higher amounts of opx crystallized in the 1210°C experiment and large amounts of spinel crystallized in subsequent steps.

Liquid compositions

Figure 5a–f displays some of the key features of the melt compositions. Selected major element abundances (expresses as wt % oxides) in quenched glasses are plotted against their degree of differentiation expressed as Mg-number [=molar Mg/(Mg/Fe), all Fe as Fe^{2+}]. Fractional and equilibrium crystallization experiments show slightly diverging differentiation trends at 0·7 GPa. SiO_2 (Fig. 5a) increases in fractional crystallization experiments in the first two differentiation steps where ol and sp, and ol, cpx and sp crystallize, followed by a rather large temperature range (1210–1090°C) where SiO_2 enrichment in the liquids is moderate (52·0–54·2 wt %). The appearance of ilm in the last fractionation step (1060°C) leads to an increase of the SiO_2 content in the liquid to 58·7 wt %. Reduced amounts of plg crystallization as well as higher proportions of sp (Fig. 3) in the equilibrium crystallization experiments result in

a continuous increase in SiO_2 between 1240°C and 1150°C, reaching 56·8 wt %. CaO contents reach their maxima at the onset of the crystallization of the first calcium-bearing phase (cpx) and, thereafter, decrease monotonically with increasing differentiation in both crystallization series (Fig. 5b). Maximum values of 12·3 wt % in fractional and 12·9 wt % in equilibrium crystallization experiments are obtained. Al_2O_3 contents initially increase in both series and reach their maximum at the onset of plg precipitation (Fig. 5c); a higher maximum is reached in equilibrium (17·0 wt %) than in fractional crystallization experiments (16·2 wt %) as a result of delayed plg crystallization. Iron, plotted as FeO_{tot} (all Fe as Fe^{2+}), and TiO_2 monotonically increase to values of 16·7 and 3·1 wt %, respectively, in fractional crystallization experiments and decrease in the last fractionation step as a result of the crystallization of ilm. With decreasing Mg-number, FeO_{tot} of the equilibrium crystallization experiments follows an evolutionary curve with a flatter slope than in the fractional crystallization experiments, whereas TiO_2 shows slightly stronger enrichment with increasing differentiation. The alkalis, Na_2O and K_2O, increase similarly for both crystallization series with increasing differentiation. The Na_2O concentrations in the liquids of the fractional crystallization experiments reach a maximum of 3·6 wt % at 1120°C. The crystallization of large fractions of sodic plagioclase leads to a slight decrease of Na_2O concentrations in the liquids between
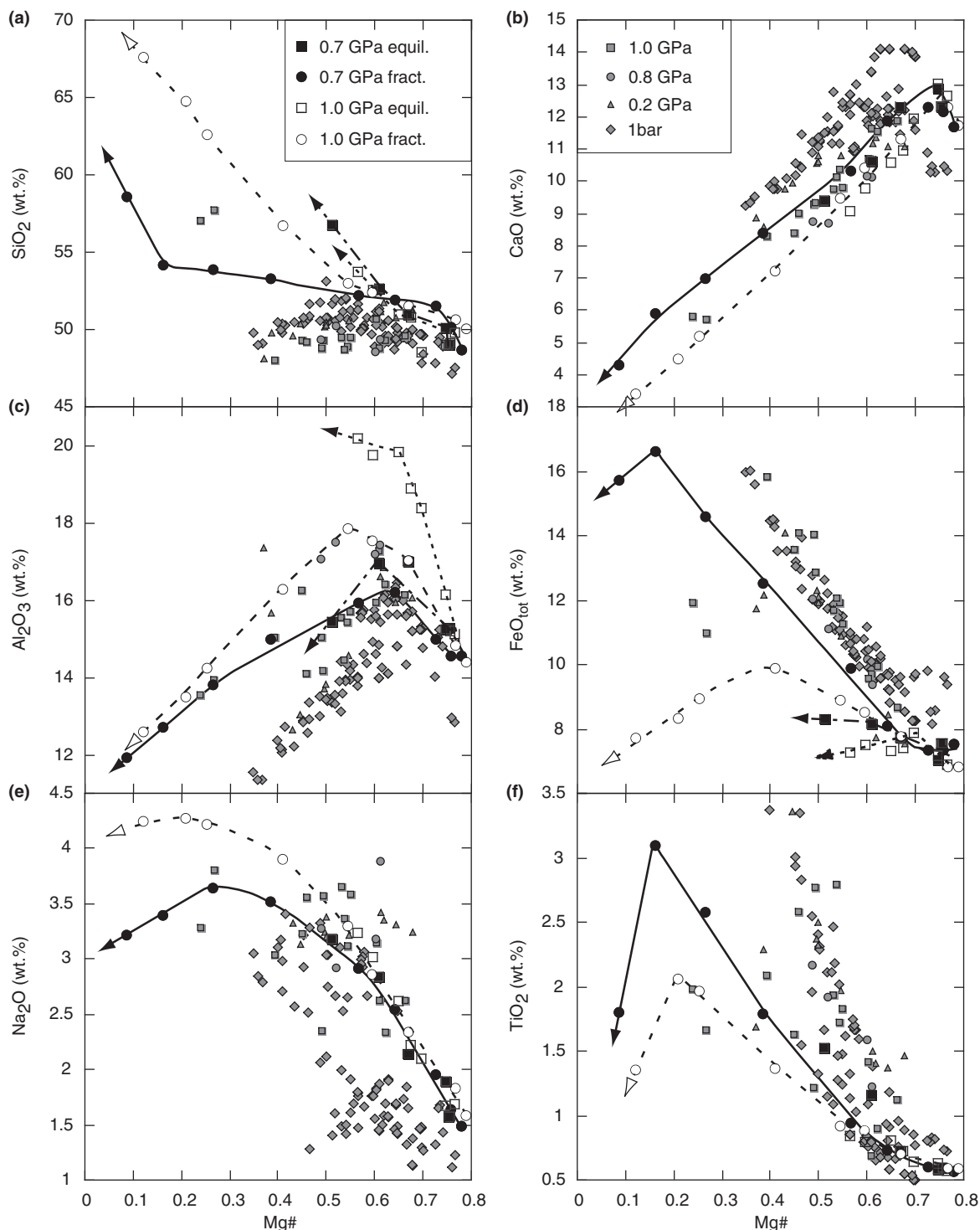
Fig. 5. Variations of selected oxides in experimental glasses in wt% plotted against Mg-number [=molar $Mg/(Mg + Fe)$] for equilibrium and fractional crystallization experiments at 0·7 GPa (filled symbols, this study) and 1·0 GPa (open symbols, Villiger *et al.*, 2004): (a) SiO_2; (b) CaO; (c) Al_2O_3; (d) FeO_{tot}; (e) Na_2O; (f) TiO_2. Experimental data from the literature (grey filled symbols) at 1 bar are taken from Grove & Bryan (1983), Tormey *et al.* (1987), Grove et al. (1990), Yang *et al* (1996), Sano *et al*. (2001) and Ulmer (unpublished data); at 0·2 GPa from Tormey *et al.* (1987) and Grove *et al.* (1992); at 0·8 GPa from Baker & Eggler (1987) and Grove *et al.* (1990, 1992); at 1·0 GPa from Fram & Longhi (1992) and Grove *et al.* (1992). Continuous lines indicate fractional crystallization trends at 0·7 GPa; dashed–dotted lines represent equilibrium crystallization trends at 0·7 GPa; long-dashed lines illustrate fractional crystallization trends at 1·0 GPa; short-dashed lines trace equilibrium crystallization trends at 1·0 GPa. Mg-number is calculated assuming all Fe as Fe^{2+}.

1120 and 1060°C. K$_2$O (not shown) behaves like a highly incompatible element, reaching 3·1 wt % at 1060°C.

Mineral compositions at 0·7 GPa

Pyroxenes

Clinopyroxene compositions are illustrated in Fig. 6a–c. Selected oxide components are plotted against Mg-number. Clinopyroxene in the fractional and equilibrium crystallization experiments changes composition in accordance with the coexisting liquid composition. The Mg-number of the clinopyroxene from the fractional crystallization experiments decreases from 0·90 to 0·26 over the temperature interval between 1240°C and 1060°C. Clinopyroxene in the equilibrium crystallization experiments shows Mg-number variation between 0·86 and 0·81 at temperatures between 1210°C and 1150°C. Al$_2$O$_3$ (Fig. 6a), TiO$_2$ (Fig. 6b) and Na$_2$O (Fig. 6c) show similar evolutionary trends for both crystallization series, with the development of bell-shaped curves exhibiting maxima in the fractional crystallization series at 4·30 wt %, 1·02 wt % and 0·38 wt %, respectively. The Al$_2$O$_3$ and Na$_2$O contents of cpx decrease with the onset of plagioclase precipitation and reach minimum values of 1·6 and 0·28 wt %, respectively, at 1060°C. The TiO$_2$ contents of the cpx decrease after the onset of ilm crystallization and reach a value of 0·93 wt % at 1060°C. Similar evolutionary trends are observed for the cpx of the equilibrium crystallization series: Al$_2$O$_3$ decreases from 5·1 to 2·5 wt % between 1210°C and 1150°C, TiO$_2$ increases from 0·25 to 0·46 wt % and Na$_2$O increases from 0·31 to 0·40 at 1180°C, followed by a decrease to 0·35 wt % at 1150°C.

Orthopyroxenes (not shown) from the equilibrium crystallization experiments contain similar amounts of Al$_2$O$_3$ to the coexisting cpx varying from 4·9 to 2·4 wt %. TiO$_2$ and Na$_2$O contents are significantly lower in the opx than in the coexisting cpx. TiO$_2$ increases with increasing differentiation from 0·14 to 0·30 wt %. In the fractional crystallization series, opx is stable with cpx in only a single experiment at 1210°C (SV97) and exhibits sector zoning. Zones of high Al$_2$O$_3$ content (4·3 wt %) also contain higher TiO$_2$ (0·14 wt %, 0·11 wt %) and Cr$_2$O$_3$ (0·56 wt %, 0·38 wt %), but are lower in SiO$_2$ (54·6 wt %, 56·1 wt %) than the zones of low Al$_2$O$_3$ (2·5 wt %). The average composition of this opx is slightly lower in Al$_2$O$_3$ (3·9 wt %) and significantly lower in TiO$_2$ (0·14 wt %) and Na$_2$O (0·04 wt %) than the coexisting cpx at a similar Mg-number.

Plagioclase

Plagioclase compositions are illustrated in the albite–orthoclase–anorthite ternary diagram (Fig. 7). Plagioclase in the fractional crystallization experiments changes from bytownite to andesine in composition ($X_{An} = 0·71–0·33$) with increasing differentiation. K$_2$O, soluble in plagioclase
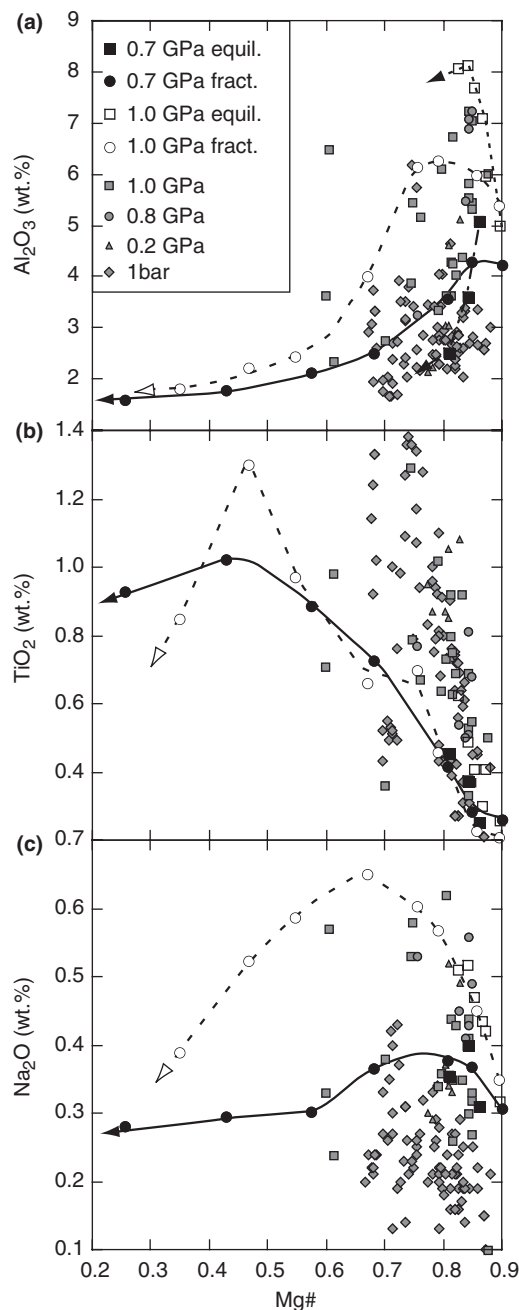
Fig. 6. Oxide variation diagrams for clinopyroxene plotted against Mg-number (all Fe as Fe^{2+}) for anhydrous experiments at 0·7 GPa (filled symbols, this study) and 1·0 GPa (open symbols, Villiger *et al.*, 2004): (a) Al$_2$O$_3$; (b) TiO$_2$; (c) Na$_2$O. Experimental cpx data from the literature (grey filled symbols): 1 bar data are from Grove & Bryan (1983), Baker & Eggler (1987), Tormey *et al.* (1987), Grove *et al.* (1990), Yang *et al.* (1996) and Sano *et al.* (2001); 0·2 GPa data from Tormey *et al.* (1987) and Grove *et al.* (1992); 0·8 GPa data from Baker & Eggler (1987) and Grove *et al.* (1990, 1992); 1·0 GPa data from Bartels *et al.* (1991), Fram & Longhi (1992) and Grove *et al.* (1992). Continuous lines indicate fractional crystallization trends at 0·7 GPa; the dashed–dotted line represents the equilibrium crystallization trend at 0·7 GPa; long-dashed lines illustrate fractional crystallization trends at 1·0 GPa; the short-dashed line traces the equilibrium crystallization trend at 1·0 GPa.
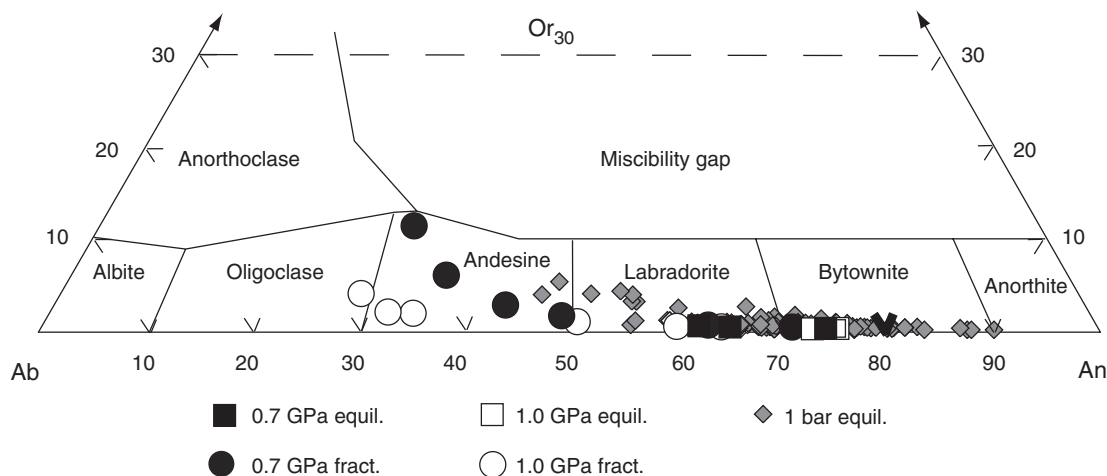
Fig. 7. Compositions of experimental plagioclase plotted as molar units in the albite–orthoclase–anorthite ternary. Plagioclase values for anhydrous fractional and equilibrium crystallization experiments at 0·7 GPa (this study) and 1·0 GPa experiments (Villiger et al., 2004) are plotted. Experimental plagioclase compositions from anhydrous experiments at 1 bar are given for comparison and are taken from Grove & Bryan (1983), Baker & Eggler (1987), Tormey et al. (1987), Grove et al. (1990), Yang et al. (1996) and Sano et al. (2001).

as the orthoclase component, increases with differentiation from 0·003 to 0·11 X_{Or}, consistent with the strongly increasing K_2O contents of the coexisting liquid phase (from 0·21 to 3·11 wt %). Plagioclases from the equilibrium crystallization show restricted ranges in X_{An} and X_{Or}, varying in the range 0·74–0·62 and 0·002–0·003, respectively.

THE EFFECT OF PRESSURE ON THE DIFFERENTIATION OF THOLEIITIC BASALTS
Phase relations
Only a limited number of experimental studies have constrained the phase equilibria of anhydrous basalts at pressures between 0·2 and 0·7 GPa (e.g. 0·2 GPa: Tormey et al., 1987; Grove et al., 1992; 0·4 GPa: Bender et al., 1978; 0·45 GPa: Green & Ringwood, 1967; 0·5 GPa: Gust & Perfit, 1987; 0·6 GPa: Bender et al., 1978). The 1 bar liquidus temperatures of these experiments vary between 1210°C and 1390°C depending on their bulk compositions. Olivine is the liquidus phase crystallizing at temperatures between 1207°C and 1380°C. These experimental studies inferred an increase of the liquidus temperature by 40–50°C over a pressure interval of 1·0 GPa. The temperature of first appearance of plagioclase in the phase assemblages varies between 1170°C and 1270°C and increases in most of the studies by 35–45°C in the range 1 bar–1·0 GPa. Green & Ringwood (1967), however, reported a negative slope of the plagioclase-in curve with an apparent temperature decrease of 50°C over 0·9 GPa. The saturation temperature of clinopyroxene varies between 1102°C and 1290°C. Experiments at 1 bar

by Gust & Perfit (1987) indicated that the cpx-in temperature is fO_2 dependent: Cpx first crystallizes at 1102°C at an fO_2 corresponding to QFM − 1 and at 1150°C under conditions corresponding to NNO +1·5. The cpx-in temperature increases by 125–145°C from 1 bar to 1·0 GPa pressure. Green & Ringwood (1967) reported a flatter slope of 50–70°C over 0·9 GPa. The flatter slope of the cpx-in curve in a pressure–temperature section relative to the ol-in and plg-in curves results in earlier crystallization of olivine and plagioclase at lower pressures with respect to cpx. The crossover of the cpx-in and plg-in curves is located between 0·5 and 0·8 GPa. Below these pressures ol + plg forms the high-temperature assemblage, producing dunitic and troctolitic cumulates. Experiments performed between 0·7 and 1·0 GPa (Green & Ringwood, 1967; Bender et al., 1978; Elthon & Scarfe, 1984; Gust & Perfit, 1987; Eggins, 1992; Grove et al., 1992; Kinzler & Grove, 1992; Villiger et al., 2004) resulted in the crystallization of clinopyroxene at similar or higher temperatures than plagioclase. Consequently, the crystallization of a primitive tholeiitic magma at pressures in excess of 0·5–0·8 GPa leads to the formation of cumulates composed of dunite followed by lherzolite, wehrlite and websterite, or directly by the crystallization of gabbroic or gabbronoritic cumulates.

Liquid lines of descent
To explore effects of pressure on the liquid lines of descent, data from equilibrium and fractional crystallization experiments at 1·0 GPa (Villiger et al., 2004), and 1 bar (Yang et al., 1996), plus the 1 bar and 1·0 GPa phase boundaries from Grove & Baker (1984), are plotted in addition to the experimental data at 0·7 GPa (this study) in Fig. 4. At 1·0 GPa the trend of projected liquids is

dominated by early fractionation/crystallization of cpx, driving liquids to low normative cpx contents. At lower pressures, enhanced olivine stability shifts the liquid compositions in the first fractionation/crystallization steps away from the olivine apex of the ol–cpx–qtz plane and leads to generally more cpx-rich liquids at a given normative qtz content. It is noteworthy that the effect of enhanced normative cpx content with decreasing pressure is much more pronounced for equilibrium than for fractional crystallization experiments. Attempts to model the liquid line of descent using the thermodynamic algorithms MELTS and pMELTS (Ghiorso & Sack, 1995; Asimow & Ghiorso, 1998; Ghiorso *et al.*, 2002) produced liquid lines of descent that are dramatically different from the experimentally derived ones, but similar to the liquid lines of descent obtained from MELTS and pMELTS at 1·0 GPa. Villiger *et al.* (2004) have extensively discussed the comparison between experimentally derived and calculated liquid lines of descent for dry tholeiitic magmas at elevated pressures and the basic conclusions remain the same. Extensive crystallization of augitic and in more advanced stages of pigeonitic cpx drives the derivative liquids in Fig. 4 away from the cpx corner and ultimately into the nepheline-normative field, outside the triangle towards the lower-left side (opposite to qtz).

Liquid compositions

To evaluate the effect of pressure on the compositional evolution of experimental liquids with differentiation, major oxide compositions of experimental liquids at 1·0 GPa (Villiger *et al.*, 2004) and equilibrium crystallization experiments between 1 bar and 1·0 GPa from the literature (for references see caption of Fig. 5) have been plotted together with the 0·7 GPa data from this study as a function of the degree of differentiation expressed as Mg-number in Fig. 5a–f. Silica (Fig. 5a) increases progressively with differentiation from basaltic to rhyodacitic compositions for fractional crystallization experiments at 1·0 GPa (Villiger *et al.*, 2004), whereas at 0·7 GPa, early SiO_2 enrichment is only observed for the equilibrium crystallization experiments. For fractional crystallization experiments at 0·7 GPa, SiO_2 increases only moderately along the liquid line of descent until a late stage when ilmenite begins to crystallize. Liquid compositions in equilibrium crystallization experiments on various starting compositions at 1 bar, 0·2 GPa, 0·8 GPa and 1·0 GPa generally have relatively low SiO_2 contents (48–53 wt %), except for two experiments at 0·8 GPa on differentiated compositions that contain 57·1 and 57·8 wt % SiO_2 (AT-29: Baker & Eggler, 1987).

CaO increases at all pressures when ol is the only liquidus phase. After the first appearance of plg at low pressures, CaO remains relatively constant (Fig. 5b).

The crystallization of cpx leads to a pronounced decrease in the CaO content. The expansion of the olivine stability field towards lower pressures results in systematically higher CaO maxima for low-pressure fractionation trends compared with higher pressure conditions. The slope of the CaO vs Mg-number trend at 0·7 GPa is slightly flatter than at 1·0 GPa, possibly because of the lower CaO contents of the crystalline phase assemblages at a given Mg-number at 0·7 GPa compared with 1·0 GPa. The variation of CaO with increasing differentiation is clearly dependent on the pressure of crystallization as shown in an accompanying study (Villiger *et al.*, 2006). The evolution of Al_2O_3 along anhydrous liquid lines of descent is dominated by the crystallization behaviour of plg: Al_2O_3 increases until first appearance of plg on the liquidus. At high pressures plagioclase appears later on the liquidus, resulting in systematically higher maxima in Al_2O_3 with increasing pressures. Lower Al contents of pyroxenes and lower plg/cpx ratios in the crystalline solid assemblage at 0·7 GPa are responsible for the flatter slope of Al_2O_3 with increasing differentiation with respect to the liquids at 1·0 GPa. Al_2O_3 contents of glasses produced at 1 bar, 0·2 GPa, 0·8 GPa and 1·0 GPa using various starting compositions define variable Al_2O_3 trends depending on both pressure and the initial Al_2O_3 content.

The variation of FeO_{tot} in the fractional crystallization experiments exhibits strongly contrasting behaviour at 1·0 and 0·7 GPa. At 1·0 GPa it reaches a maximum at <10·0 wt %. FeO_{tot} starts to decrease when the sum of FeO in the solid phase assemblage exceeds the amount of FeO in the coexisting liquid (Villiger *et al.*, 2004). At 0·7 GPa, FeO_{tot} reaches a maximum of 16·7 wt % and only slightly decreases in the last fractionation step when significant amounts of ilmenite crystallize. Except for the first (and last) fractionation step the calculated cumulate compositions do not exceed the FeO content of the coexisting liquids. Liquid compositions from equilibrium crystallization experiments taken from the literature at 1 bar, 0·2, 0·8 and 1·0 GPa evolve along a trajectory of increasing FeO_{tot} with differentiation that is steeper than for either the fractional or equilibrium crystallization experiments at 0·7 and 1·0 GPa on composition HK19 (this study). The starting compositions of the former studies contain higher FeO_{tot} at a given Mg-number than the starting composition (HK19) of our experiments. Two experimental glasses produced at 0·8 GPa on differentiated compositions (AT-29: Baker & Eggler, 1987) plot between the 1·0 GPa and 0·7 GPa fractional crystallization experiments and four glasses at 0·2 GPa (Tormey *et al.*, 1987) plot near the fractional crystallization trends at 0·7 GPa.

Na_2O becomes progressively enriched in the liquid phase with increasing differentiation for fractional and

equilibrium crystallization experiments until the solid phase assemblage becomes more Na_2O-rich than the coexisting liquid, resulting in a slight to moderate decrease of the Na_2O content in the last crystallization steps. Sodium contents in the melt reach higher values at 1·0 GPa (4·28 wt %) than at 0·7 GPa (3·65 wt %). Na_2O contents of equilibrium crystallization experiments at 1 bar, 0·2 GPa and 0·8 GPa using different starting compositions scatter between 1·0 and 3·8 wt % at a Mg-number of 0·6, clearly indicating that the Na_2O content of the starting composition dominates the Na_2O evolution in differentiated liquids. Experimental problems arising from Na loss during the experiments, which has been reported for some 1 bar experiments, as well as analytical difficulties caused by Na_2O loss during electron microprobe analysis of Na-rich glasses pose additional problems for the interpretation of the Na_2O vs Mg-number evolution diagram.

TiO_2 behaves as an incompatible element over most of the differentiation history: it increases moderately before plg crystallizes. The crystallization of the TiO_2-free phase (plg) results in a more rapid increase of TiO_2 in the melt phase of the fractional crystallization experiments until the onset of ilmenite crystallization. The maximum TiO_2 content attained in the differentiation trend at 0·7 GPa is considerably higher than at 1·0 GPa, most probably related to the earlier saturation of plg and the lower TiO_2 contents of the pyroxenes. Equilibrium crystallization experiments with different bulk compositions at 1 bar, 0·2 GPa, 0·8 GPa and 1·0 GPa follow different TiO_2 trends controlled by their initial composition and phase relations.

Clinopyroxene compositions

The Al_2O_3 content of clinopyroxene (Fig. 6a) increases concomitantly with that of the liquid until plagioclase co-precipitates and decreases thereafter. It reaches higher maxima at 1·0 GPa (6·2 and 8·1 wt % for fractional and equilibrium crystallization, respectively) than at 0·7 GPa, where cpx attains 4·3 and 5·1 wt % Al_2O_3 for fractional and equilibrium crystallization experiments. Cpx from equilibrium crystallization experiments at 1 bar, 0·2 GPa, 0·8 GPa and 1·0 GPa on different bulk compositions taken from the literature show variable Al_2O_3 trends, mainly correlating with pressure (plg$_{in}$-temperature) and the Al_2O_3 content of their coexisting liquids.

TiO_2 contents of cpx increase for both fractional and equilibrium crystallization experiments at 1·0 and 0·7 GPa with increasing differentiation (Fig. 6b). Only in the last steps of the fractionation experiments at both 0·7 and 1·0 GPa is a marked decrease of the TiO_2 concentrations in cpx observed. This coincides with the onset of ilmenite crystallization. Despite the lower TiO_2 contents in the coexisting liquids, the TiO_2 content of cpx at

1·0 GPa reaches higher values of up to 1·3 wt % compared with cpx at 0·7 GPa (1·0 wt %). Consequently, this results in higher Ti partition coefficients between pyroxene and coexisting melts at 1·0 GPa than at 0·7 GPa (see next section). The TiO_2 contents of cpx in equilibrium crystallization experiments at 1 bar, 0·2 GPa, 0·8 GPa and 1·0 GPa (reported in the literature) that were conducted on variable starting compositions show different amounts of TiO_2 predominantly depending on the bulk composition of the starting material.

The Na_2O contents of cpx evolve similarly for fractional and equilibrium crystallization experiments, reaching maximum concentrations at the onset of plg crystallization (Fig. 6c). Cpx from experiments performed at 1·0 GPa contains higher concentrations of Na_2O at a comparable Mg-number than cpx at 0·7 GPa, reflecting the increasing jadeite ($NaAlSi_2O_6$) component with increasing pressure. Literature data on cpx from experiments at 1 bar, 0·2 GPa, 0·8 GPa and 1·0 GPa support the general observation that the Na_2O contents of cpx are higher for higher pressure experiments. Different trends at identical pressures suggest that the Na_2O contents of the cpx are also dependent on the bulk composition of the starting material.

Plagioclase compositions

Plagioclase compositions from the 0·7 and 1·0 GPa experiments are plotted together with 1 bar data (data sources given in caption of Fig. 7) in a molar albite–orthoclase–anorthite diagram in Fig. 7. Plagioclase compositions vary between An_{75} and An_{29} for the high-pressure experiments and reach An_{90} for the 1 bar experiments. In the fractional crystallization experiments, we observed a significant increase in the Or component with decreasing pressure for highly differentiated compositions. Increased K_2O contents, exceeding the values for the 0·7 and 1·0 GPa data, are also observed for intermediate plagioclase compositions at 1 bar, indicating a general trend of increasing K_2O contents with decreasing pressure.

Mineral–liquid exchange reactions
Clinopyroxene

The partition coefficients for Al_2O_3, TiO_2 and Na_2O between clinopyroxene and coexisting liquid are listed in Table 4. Figure 8a–c displays the logarithms of the clinopyroxene–liquid distribution coefficients for these oxides (log Al_2O_3 $K_d = \log[Al_2O_3(pyx)/Al_2O_3(liq)]$) as functions of the inverse temperature (K) and their calculated activities in the melt phase.

Logarithms of Al_2O_3 partition coefficients at 0·7 GPa decrease with decreasing temperature after the onset of plagioclase crystallization from −0·55 to −0·87. The Al K_d values of fractional and equilibrium crystallization experiments at 0·7 GPa follow a trend similar to that observed
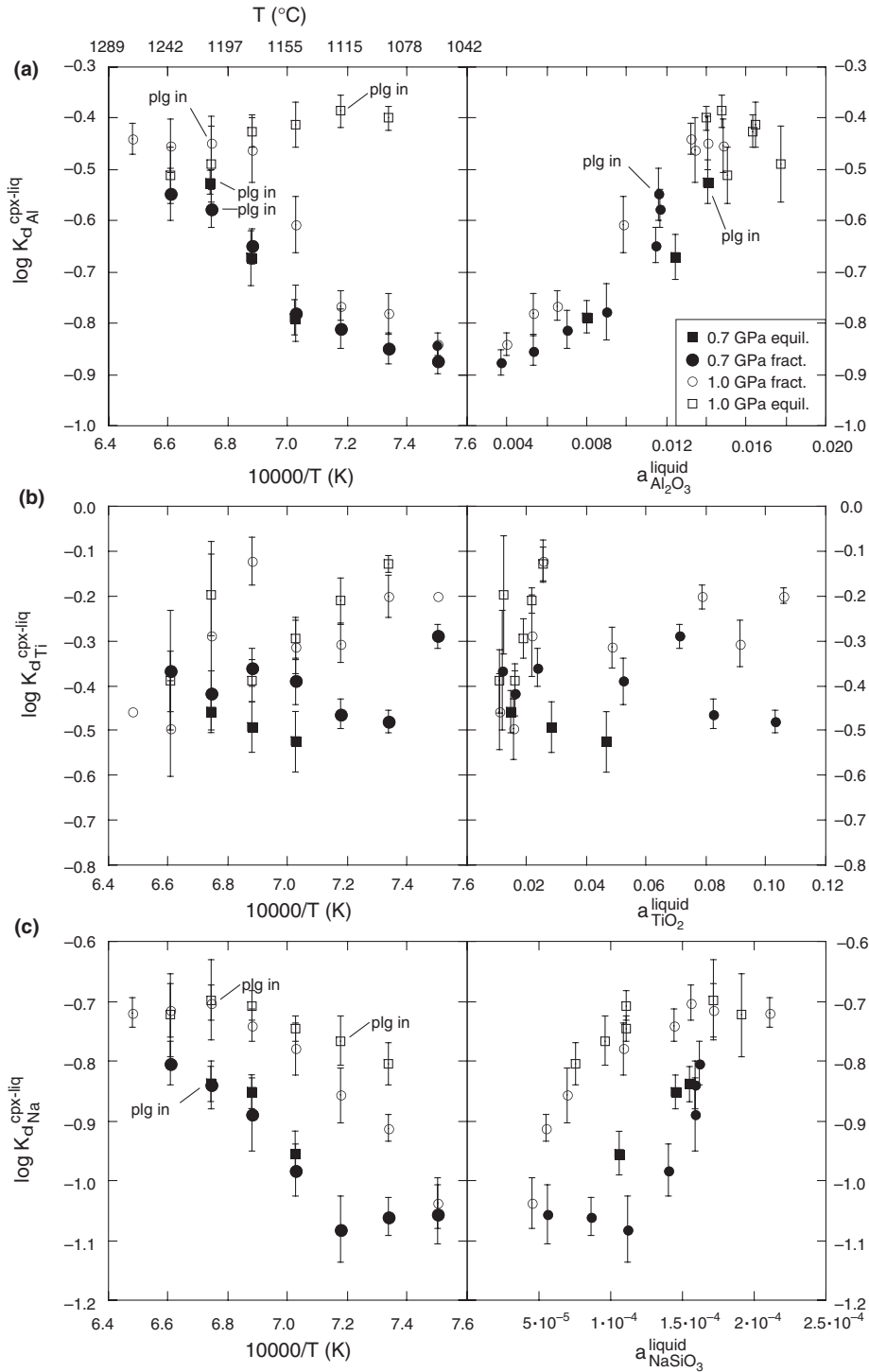
**Fig. 8.** Logarithm of (a) Al_2O_3, (b) TiO_2 and (c) Na_2O partition coefficients (log K_d) between clinopyroxene and liquid as functions of reciprocal temperature (K^{-1}) and calculated Al_2O_3 (a), TiO_2 (b) and $NaSiO_3$ (c) activities in the liquid phase for equilibrium and fractional crystallization experiments at 1·0 GPa (Villiger *et al.*, 2004) and 0·7 GPa pressure (this study). The activities of components in the melt phase were calculated for each experimental glass composition using the MELTS Supplemental Calculator (Ghiorso & Sack, 1995; Asimow & Ghiorso, 1998) at 0·7 GPa and 1·0 GPa and their respective experimental temperatures (1330–1060°C).

for the fractional crystallization experiments at $1.0\,GPa$ (-0.44 to -0.84), but displaced to lower values, unlike the $1.0\,GPa$ equilibrium crystallization experiments where Al K_d increases with differentiation as a result of the delayed crystallization of plagioclase (Villiger et al., 2004). The possible dependence of the Al partitioning behaviour on the liquid composition was tested by calculating the Al_2O_3 and SiO_2 activities of the liquids with the supplemental calculator provided on the MELTS web page of Mark Ghiorso (http://CTserver.uchicago.edu) at the pressure–temperature conditions of the experiments. The calculated Al_2O_3 activities are plotted in Fig. 8a as a function of log Al K_d. A clear positive correlation exists between the Al_2O_3 pyroxene–liquid K_d and the calculated Al_2O_3 activities of the liquid phases of fractional and equilibrium crystallization experiments at $0.7\,GPa$ as observed by Villiger et al. (2004) for $1.0\,GPa$. These observations reinforce previous statements that the partitioning of Al_2O_3 between coexisting liquid and pyroxene is strongly controlled by the thermodynamic properties of the liquid phase (Villiger et al., 2004). The complementary behaviour of the variation of log K_d with the calculated alumina and silica activities (not shown) of the liquid phase is consistent with a control by the Tschermak's component in cpx (Fe^{2+}, Mg or $CaAl_2SiO_6$ component in cpx) and by the activity of the Tschermak's component in the liquid phase, which in turn is related to the variable onset of plagioclase crystallization at 0.7 and $1.0\,GPa$ in the fractional and equilibrium crystallization experiments.

The TiO_2 distribution coefficients (log K_d pyx–liq) plotted against the reciprocal temperature and calculated TiO_2 activities in the liquid phase scatter between -0.29 and -0.48 for fractional and -0.46 and -0.52 for equilibrium crystallization experiments (Fig. 8b). The average log K_d values for fractional (-0.12 to -0.50) and equilibrium crystallization experiments (-0.13 to -0.39) are higher at 1.0 than at $0.7\,GPa$. We did not observe any systematic correlation with either the temperature or Ti activity of the coexisting liquid phases. Ti incorporation in pyroxene is mainly controlled by crystal chemical parameters and is often taken as an analogue for the behaviour of high field strength elements (HFSE; Kelemen et al., 1990; Forsythe et al., 1994). TiO_2 contents generally correlate positively with Al^{IV} in cpx (Lundstrom et al., 1998; Hill et al., 2000; Wood & Trigila, 2001) and Ti is incorporated as the $CaTiAl_2O_6$ molecule (Onuma & Yagi, 1971; Akella & Boyd, 1972) through a coupled substitution $Ti^{4+[VI]} + 2\ Al^{[IV]} = R^{2+[VI]} + 2\ Si^{[IV]}$ (Verhoogen, 1962). Figure 9a shows that the log K_d values of TiO_2 between cpx and liquid roughly correlate with the SiO_2/Al_2O_3 ratios of the liquids at $0.7\,GPa$ (this study) and $1.0\,GPa$ (Villiger et al., 2004) and the anhydrous experiments between 1 bar and $1.0\,GPa$
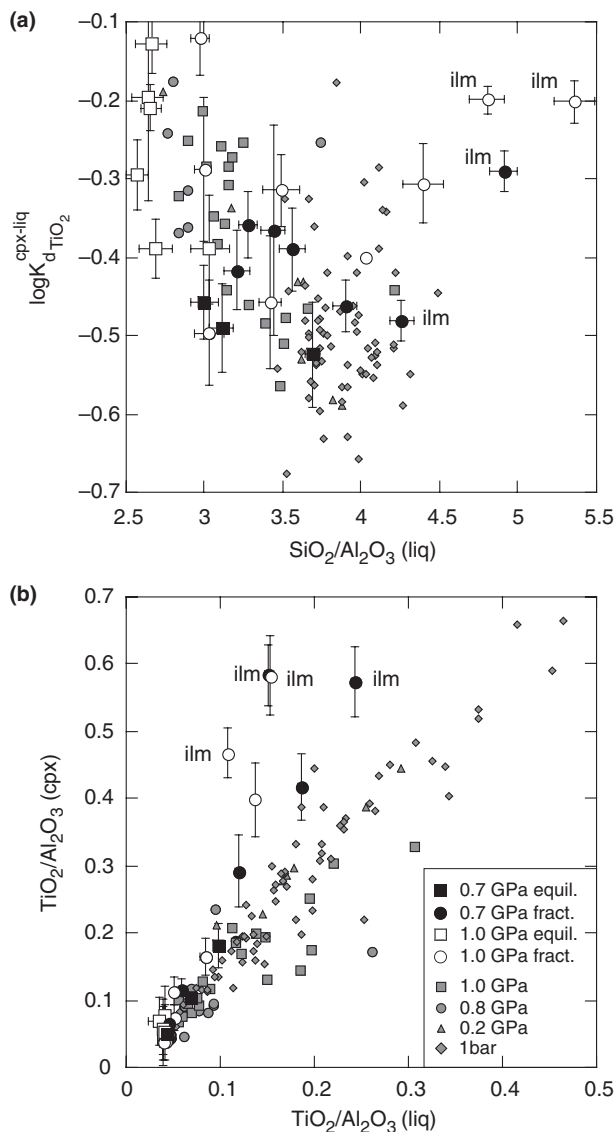
Fig. 9. (a) Logarithm of the TiO_2 partition coefficients (log K_d) between clinopyroxene and liquid as a function of the SiO_2/Al_2O_3 ratio of the liquid; (b) TiO_2/Al_2O_3 ratios of clinopyroxene as a function of the TiO_2/Al_2O_3 ratio of coexisting liquids. Data for equilibrium and fractional crystallization experiments at $1.0\,GPa$ (Villiger et al., 2004) and at $0.7\,GPa$ (this study) are plotted. Data sources for anhydrous equilibrium crystallization experiments at 1 bar, $0.2\,GPa$, $0.8\,GPa$ and $1.0\,GPa$ are as in Fig. 6.

(data sources are given in the caption of Fig. 6). The most differentiated cpx–glass pairs in the fractional crystallization experiments at $0.7\,GPa$ and $1.0\,GPa$ display an inversion of the overall negative correlation with the SiO_2/Al_2O_3 ratio. The solid assemblages in these experiments contain ilmenite (Fig. 9a). Figure 9b illustrates the variation of TiO_2/Al_2O_3 ratios in cpx as a function of the TiO_2/Al_2O_3 ratios of coexisting liquids. A nearly linear positive trend is observed for most experiments, with the exception

of the fractional crystallization experiments at 0·7 GPa and 1·0 GPa that define a steeper trend than the equilibrium crystallization experiments from the literature. This deviation from the general trend most probably reflects the higher Al_2O_3 contents of the glasses (lower TiO_2/Al_2O_3) produced by fractional crystallization at similar Mg-number compared with equilibrium crystallization experiments. The dependence of the pyroxene Ti solubility on the Al_2O_3 content of coexisting liquids has been reported by Thompson (1974) and Forsythe *et al.* (1994).

The Na distribution coefficients of the fractional crystallization experiments at 0·7 GPa (Fig. 8c) decrease with decreasing temperature and decreasing $NaSiO_3$ activities in the liquid from −0·80 to −1·08, except for the last two steps of fractionation where a slight increase to −1·06 is observed; this occurs despite a continuous decrease of the sodium concentrations in clinopyroxene. The log Na-K_d of equilibrium crystallization experiments follows a similar trend decreasing from −0·84 to −0·96. At 1·0 GPa, an initial increase from −0·72 to −0·70 is followed by continuous decrease of the log Na-K_d pyx–liq to −0·80 in equilibrium and with a steeper slope for the fractional crystallization experiments to −1·04. Log Na-K_d as a function of $NaSiO_3$ activity decreases for both series at 1·0 GPa after the onset of plg crystallization. The shift of the Na-K_d to higher values at 1·0 GPa compared with 0·7 for a given $NaSiO_3$ activity in the liquid indicates that increasing jadeite ($NaAlSi_2O_6$) component of cpx as a function of pressure is an important parameter controlling the Na_2O content of the cpx in our experiments.

Figure 10a displays the average values of experimental cpx–liquid Na-K_d as a function of pressure from these experiments combined with a large number of literature data (references are given in the captions of Fig. 10). The Na-K_d values obtained from piston cylinder experiments conducted in graphite–platinum capsules range from 0·06 at 0·5 GPa to 0·86 at 3·0 GPa. The data have been fitted by an exponential function shown as a continuous curve in Fig. 10a and given as the equation

$$K_{d\,Na}^{cpx-liq} = 0·063852 \times \exp[0·85036 \times P(GPa)]. \quad (1)$$

The average K_d observed at 1 bar and 0·2 GPa is 0·09. The 1 bar experiments were performed in gas mixing furnaces at fO_2 corresponding to the FMQ or NNO equilibria. The 0·2 GPa experiments were performed in internally heated hydrothermal apparatus using Pt_{90}–Fe_{10} capsules assuming fO_2 close the FMQ buffer. Toplis *et al.* (1994) investigated the effect of fO_2 on the Na partitioning between clinopyroxene and liquid. The Na-K_d values show an increase at fO_2 conditions higher than FMQ related to the incorporation of Na as an acmite ($NaFe^{3+}Si_2O_6$) component in addition to the jadeite
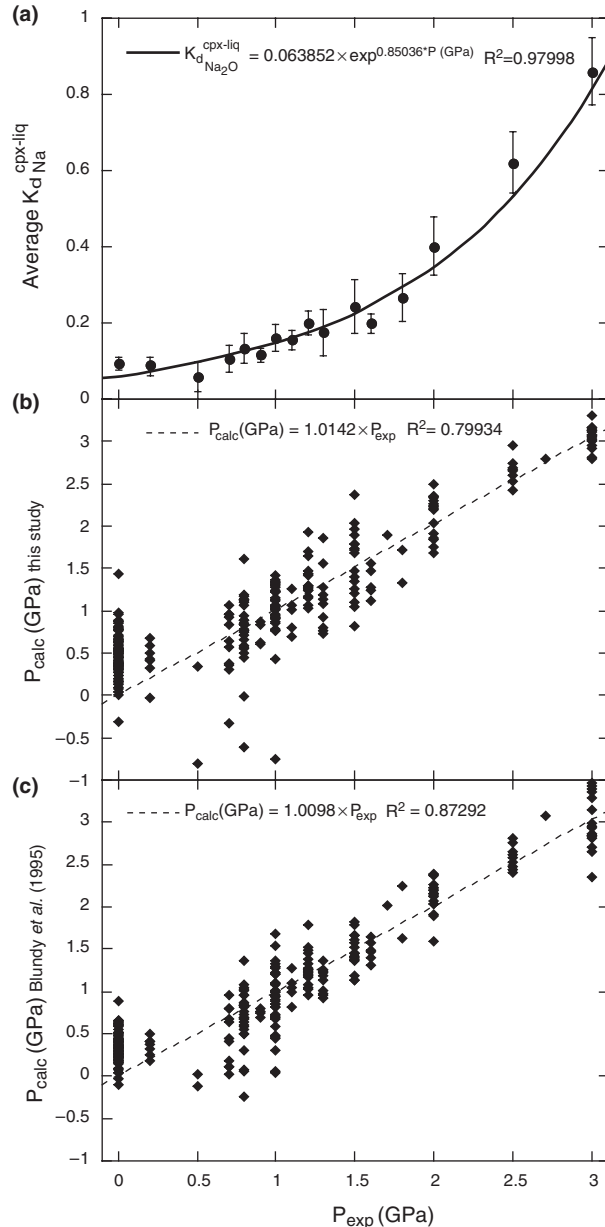
Fig. 10. (a) Average cpx–liquid K_d for Na_2O vs experimental pressure (GPa); (b) pressures calculated with equation (2) plotted against experimental pressures (GPa); (c) pressures calculated with equation (4) (Blundy *et al*, 1995) plotted against experimental pressure (GPa). Data for anhydrous experiments in the pressure range between 1 bar and 3·0 GPa are taken from Bender *et al.* (1978), Grove & Bryan (1983), Elthon & Scarfe (1984), Baker & Eggler (1987), Tormey *et al.* (1987), Grove *et al.* (1990, 1992), Bartels *et al.* (1991), Fram & Longhi (1992), Kinzler & Grove (1992), Baker *et al.* (1994), Panjasawatwong *et al.* (1995), Putirka *et al.* (1996), Yang *et al.* (1996), Johnson (1998), Thy *et al.* (1999), Sano *et al.* (2001), Pertermann & Hirschmann (2003), Villiger *et al.* (2004) and this study. Error bars (Fig. 10a) indicate standard deviations at a given pressure. The lines represent fitted curves using exponential (a), and linear (b) and (c) functions, respectively.

component ($NaAlSi_2O_6$) that dominates at low fO_2 conditions. Na loss is reported for most of the 1 bar experiments; this could also influence the Na partitioning provided the Na loss occurred preferentially from the liquid phase during late stages of the experiments.

Equation (1) has been rearranged to obtain the equation

$$P(GPa) = \frac{\ln K_{d\,Na}^{cpx-liq}}{0 \cdot 85036} + 3 \cdot 2353208 \qquad (2)$$

that was used to calculate pressures from cpx–liquid Na partition coefficients. Figure 10b shows calculated vs experimental pressures. Blundy et al. (1995) have discussed the pressure and temperature dependence of Na partitioning between melt and clinopyroxene. Based on the jadeite melting reaction, their empirical formulation of the Na partitioning between cpx and liquid,

$$K_{d\,Na}^{cpx-liq} = \exp\left(\frac{10367 + 2100 \times P - 165 \times P^2}{T} \right.$$
$$\left. - 10 \cdot 27 + 0 \cdot 358 \times P - 0 \cdot 0184 \times P^2 \right) \qquad (3)$$

exhibits increasing K_d with increasing pressure, but also decreasing K_d with increasing temperature. For comparison, equation (3) was solved for pressure (GPa) and the solution,

than at $1 \cdot 0$ GPa (see Fig. 7). Therefore, we have used the $CaO/(Na_2O + K_2O)$ ratio (expressed in wt %) between plagioclase and liquid in Fig. 11 instead of the CaO/Na_2O ratio used by Villiger et al. (2004). The positive correlation of the CaO/Na_2O ratio at constant H_2O demonstrated experimentally by Sisson & Grove (1993) and Berndt et al. (2005) is also valid for $CaO/(Na_2O + K_2O)$ ratios but at slightly different values. Sisson & Grove (1993) reported increasing K_d $[=(CaO/Na_2O)_{plg}/(CaO/Na_2O)_{liq}]$ with increasing H_2O content in the melt phase. The $CaO/(Na_2O + K_2O)$ of plagioclase plotted against the $CaO/(Na_2O + K_2O)$ of the liquids of the equilibrium and fractional crystallization experiments at $0 \cdot 7$ GPa defines a linear function with a slope similar to the fractional crystallization experiments at $1 \cdot 0$ GPa (Fig. 10). The slope defines an average $CaO/(Na_2O + K_2O)$ K_d between plg and melt of $0 \cdot 94 \pm 0 \cdot 08$ for fractional crystallization experiments at $0 \cdot 7$ GPa and $1 \cdot 05 \pm 0 \cdot 14$ at $1 \cdot 0$ GPa. The average K_d of the equilibrium crystallization experiments at $0 \cdot 7$ GPa is $1 \cdot 00 \pm 0 \cdot 09$ and $1 \cdot 83 \pm 0 \cdot 04$ at $1 \cdot 0$ GPa. Our data fall within the range of K_d of 226 nominally anhydrous experiments taken from the literature that cover the pressure range from 1 bar to $1 \cdot 5$ GPa. The total variation of all the experimental data is from $0 \cdot 67$ to $2 \cdot 36$ with an average value of $1 \cdot 19 \pm 0 \cdot 30$ (references for experiments

$$P_{1/2} = \frac{\dfrac{2100 + 0 \cdot 358 \times T}{-165 - 0 \cdot 0184 \times T}}{2}$$
$$\pm \sqrt{\frac{[(2100 + 0 \cdot 358 \times T)/(-165 - 0 \cdot 0184 \times T)]^2}{4} - \frac{10367 + T \times (-10 \cdot 27 - \ln K_{d\,Na}^{cpx-liq})}{-165 - 0 \cdot 0184 \times T}} \qquad (4)$$

was used to calculate pressures that are compared in Fig. 10c with the experimental pressures. There is no fundamental improvement by incorporating temperature as an additional variable to pressure (Fig. 10b compared with 10c). Therefore, we conclude that with the currently available dataset, a clear relationship between Na partitioning and temperature cannot be established. Our experimental dataset covers a large range of compositions and most probably implies that, in addition to the strong pressure dependence, a compositional effect and an effect depending on the phase assemblage coexisting with cpx and melt cannot be ruled out and is potentially more important than the inferred temperature dependence.
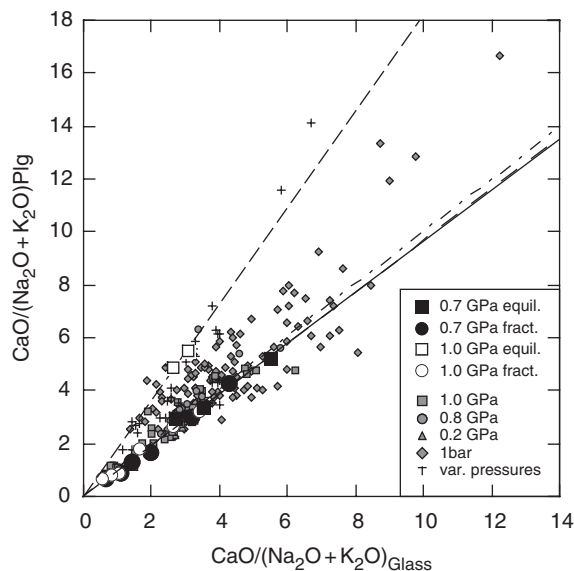
Plagioclase

Potassium becomes a much more important component in feldspars under fractional crystallization at $0 \cdot 7$ GPa

are given the caption of Fig. 11). In contrast to Fram & Longhi (1992), Grove et al. (1992), Sisson & Grove (1993) and Panjasawatwong et al. (1995), who invoked either negative or positive correlation of the plg–liq K_d with pressure, the dataset we have used here (Fig. 11) does not show any systematic pressure or temperature correlation over the range $0-1 \cdot 5$ GPa and $1050-1300°C$.

DISCUSSION AND CONCLUSIONS

The results of this experimental study, performed at $0 \cdot 7$ GPa and $1060-1270°C$, provide constraints on phase equilibria and the compositions of liquids and residual solids along the liquid lines of descent of anhydrous, mantle-derived primary magmas. The two contrasting series of experiments, simulating equilibrium (closed-system) and fractional (open-system) crystallization result in contrasting evolutionary trends. Liquids

Fig. 11. $CaO/(Na_2O + K_2O)$ (wt %) of plagioclase vs that of coexisting liquid (quenched glass) in equilibrium and fractional crystallization experiments at 0·7 GPa and at 1·0 GPa (this study; Villiger *et al.*, 2004). Experimental data are taken from the literature: 1 bar data are from Bender *et al.* (1978), Grove & Bryan (1983), Tormey *et al.* (1987), Grove *et al.* (1990), Bartels *et al.* (1991), Baker *et al.* (1994), Yang *et al.* (1996), Thy *et al.* (1999) and Sano *et al.* (2001); 0·2 GPa data from Grove *et al.* (1992); 0·8 GPa data from Bender *et al.* (1978), Baker & Eggler (1987) and Grove *et al.* (1990, 1992); 1·0 GPa data from Bartels *et al.* (1991), Grove *et al.* (1992) and Panjasawatwong *et al.* (1995). Crosses represent additional data taken from anhydrous experiments at 0·5 GPa (Panjasawatwong *et al.* 1995); at 0·9 GPa and 1·3 GPa (Kinzler & Grove (1992); and at 1·1 GPa, 1·2 GPa and 1·5 GPa (Bartels *et al.*, 1991).

in the fractional crystallization experiments evolve similarly to those of typical tholeiitic magma series: a moderate silica increase from basalt to basaltic andesite, paired with a strong Fe enrichment, followed by very late-stage SiO_2 enrichment related to the extraction of ilmenite. In contrast, liquids in the equilibrium crystallization experiments at 0·7 GPa, as well as in all experiments at 1·0 GPa (Villiger *et al.*, 2004), evolve more like calc-alkaline series magmas, with progressive SiO_2 enrichment and only moderate Fe enrichment. The latter, however, is related to closed-system behaviour in the equilibrium crystallization experiments that limits any Fe enrichment to Mg-number >0·5. The change of Al_2O_3 and CaO concentrations along the liquid lines of descent is clearly related to pressure. Principal phase equilibria controls are responsible for their contrasting trends. Earlier plagioclase saturation in the experiments at 0·7 GPa compared with the experiments at 1·0 GPa results in lower Al_2O_3 contents of the liquids produced at 0·7 GPa. The expansion of the olivine stability field relative to cpx at lower pressures results in a higher CaO maximum on the liquid line of descent. In contrast

to tholeiitic differentiation trends at low pressure (1 bar), suppressed plagioclase crystallization and the persistence of spinel crystallization cause continuous silica enrichment at 1·0 GPa and in the equilibrium crystallization experiments at 0·7 GPa with increasing differentiation. As a consequence, crystallization processes operating in the lower continental crust or even within the uppermost mantle below mid-ocean ridges (0·7–1·0 GPa pressure, equivalent to ~20–35 km depth) lead to the production of large volumes of ultramafic cumulates, 4–28 wt % at 0·7 GPa, consisting of dunites, wehrlites and plg-bearing websterites followed by gabbroic assemblages (gabbronorites and/or gabbros). The main difference from the experiments at 1·0 GPa that produce 34–47 wt % of ultramafic cumulates is the absence of spinel websterites at 0·7 GPa that form prior to gabbroic assemblages at 1·0 GPa.

Figure 12 displays the results (reported in Table 5) of empirical calculations of the density of the liquids coexisting with solid phases at each temperature and pressure in the equilibrium and fractional crystallization experiments, computed using the algorithms of Lange & Carmichael (1987) and Lange (1994) for anhydrous conditions and for an initial H_2O content of 1000 ppm in the primary liquid (HK#19). To assess the probability that primary and differentiated liquids and/or magmas ascend from lower crustal reservoirs, the density contrasts with their surrounding wall-rocks, as well as the density contrast with the lithologies forming the middle and upper crust are important rheological parameters provided that the overall tectonic regime is extensional as is often the case when tholeiitic melts are formed through decompression of asthenospheric mantle. For comparison, densities of typical lower to middle crustal lithologies are also shown (Fig. 12). For felsic to intermediate crustal rocks average modal granite, granodiorite and tonalite compositions were taken from the Adamello batholith (Bianchi *et al.*, 1970) and for mafic and pelitic crustal rocks modal abundances for hornblende and pyroxene gabbros and granulites and garnet–feldspar–biotite–sillimanite metapelites were taken from the Ivrea Zone (Schmid & Wood, 1976). Densities were calculated at conditions of 0·7 GPa, 650°C and 1·0 GPa, 800°C using the algorithm provided by Hacker & Abers (2004). Felsic igneous rocks (granites or granodiorites) have densities of 2·69–2·72 g/cm³, intermediate rocks (tonalites) 2·83 g/cm³, amphibole gabbros and amphibolite-facies metapelites range from 2·92 to 2·97, and pyroxene–ol-gabbros and granulite-facies metapelites (residual after granite melt extraction) have high densities of 3·14–3·22 g/cm³. In the case of completely anhydrous magmas only liquids produced by fractional crystallization at high pressure, exceeding 0·7 GPa (i.e. in magma
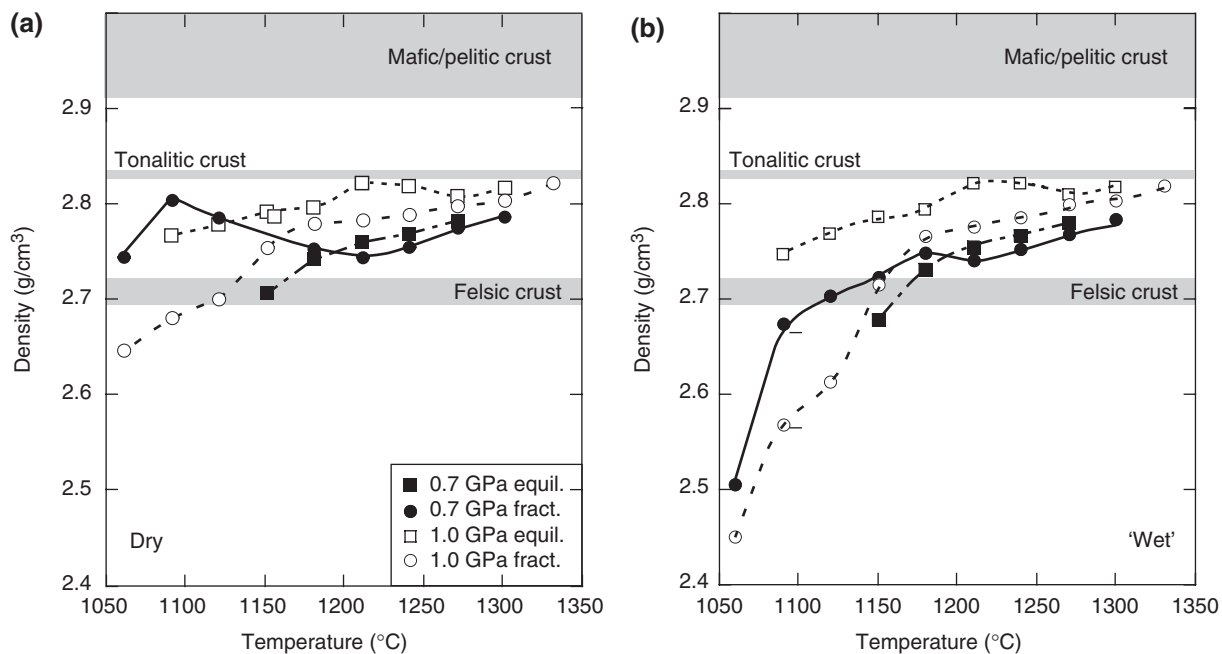
Fig. 12. Variation of calculated densities (g/cm^3) of experimental liquids as a function of temperature (°C). (a) Densities of anhydrous liquids from equilibrium and fractional crystallization experiments at 0·7 GPa (this study) and 1·0 GPa (Villiger *et al.*, 2004) calculated with the method of Lange & Carmichael (1987) and Lange (1994). Partial molar volumes of the liquid oxide components have been calculated at the experimental temperatures and pressures. (b) Calculated densities of hydrous experimental liquids assuming an initial H_2O content of the primary liquids (HK#19, 19.1 or 19.2; see Table 1) of 0·1 wt % (1000 ppm). Water is assumed to behave as a perfectly incompatible element over the entire range of temperature investigated. Results of density calculations and accumulated H_2O contents are given in Table 5. Densities of typical lower to middle crustal rocks are given for comparison and indicated by grey bars. For felsic and intermediate crustal rocks, average modal granite, granodiorite and tonalite compositions were taken from the Adamello batholith (Bianchi *et al.*, 1970) and for mafic and pelitic crustal rocks modal abundances for hornblende and pyroxene gabbros and granulites and garnet–feldspar–biotite–sillimanite metapelites were taken from the Ivrea Zone (Schmid & Wood, 1976). Densities were calculated at conditions of 0·7 GPa, 650°C and 1·0 GPa, 800°C using the algorithm of Hacker & Abers (2004).

reservoirs located at depths greater than ∼25 km), reach densities low enough to ascend to shallow levels. Low-temperature residual liquids representing rhyodacitic to rhyolitic compositions attain densities of less than ∼2·7 g/cm^3, which are typical for amphibolite-facies felsic compositions forming the middle and upper crust. Therefore, under completely dry conditions, magmas are able to ascend into and through the granulite-facies mafic to pelitic lower crust, but only differentiation within the lower part of the crust can provide liquids that can ascend to shallower levels of the crust to form granodioritic to granitic plutonic and/or rhyodacitic to dacitic sub-volcanic to volcanic complexes. Similar conclusions were reached by Herzberg *et al.* (1983) basing on theoretical considerations of relative magma and crustal rock densities. The fractionation experiments at 0·7 GPa show the characteristic density distribution of typical tholeiitic magmas (e.g. Sparks *et al.*, 1980; Stolper & Walker, 1980) with a trough in the middle range and an increase to Fe-rich liquids prior to the crystallization of Fe–Ti-oxide that decreases the density of highly differentiated granitic liquids in the last differentiation step performed in this experimental study.

Provided that the addition of small amounts of H_2O (0·1 wt %) to the primary liquid does not fundamentally alter the differentiation path until about 1 wt % of H_2O is reached in the liquid phase, all experiments, except the lowest three differentiation steps at 0·7 and 1·0 GPa (1060–1120°C), should not be dramatically affected by this assumption. Figure 12b shows that the addition of small amounts of H_2O to the primary liquid mainly lowers the density (and the viscosity, not shown) of the liquids formed in the latest differentiation steps. This leads to the formation of 'low-density' liquids in fractionated tholeiitic basalts at both 0·7 and 1·0 GPa as a result of the large amount of H_2O (>3·0 wt %) in the highly differentiated liquids, reflecting the profound effects of H_2O on the density of silicate liquids (Burnham, 1971). Similar to the observations of Grove & Baker (1983), the accumulation of H_2O in the liquid with progressive differentiation compensates the Fe enrichment effect of increasing density prior to Fe–Ti oxide precipitation in the fractional crystallization experiments at 0·7 GPa. Fractional crystallization results in highly differentiated liquids representing small melt fractions compared with the initial liquid mass; these liquids

Table 5: Calculated densities of liquid compositions for fractional and equilibrium crystallization experiments at 0·7 GPa (this study) and 1·0 GPa (Villiger et al., *2004)*

Run no.	P (GPa)	T (°C)	MF$_{acc.}$	H$_2$O$_{theor.}$ (wt%)	ρ_{dry} (g/cm^3)	ρ_{wet} (g/cm^3)
Fractional crystallization at 0·7 Gpa						
HK19.2	0·7	1300	1·000	0·10	2·78	2·78
SV76	0·7	1270	0·940	0·11	2·77	2·77
SV96	0·7	1240	0·827	0·12	2·75	2·75
SV97	0·7	1210	0·578	0·17	2·74	2·74
SV99	0·7	1180	0·395	0·25	2·75	2·75
SV101	0·7	1150	0·156	0·64	2·75	2·72
SV103	0·7	1120	0·093	1·08	2·78	2·70
SV104	0·7	1090	0·060	1·66	2·80	2·67
SV107	0·7	1060	0·032	3·14	2·74	2·51
Equilibrium crystallization at 0·7 GPa						
HK#19.1	0·7	1270	1·000	0·10	2·78	2·78
SV75	0·7	1240	0·957	0·10	2·76	2·77
SV89	0·7	1210	0·715	0·14	2·76	2·75
SV90	0·7	1180	0·458	0·22	2·74	2·73
SV79	0·7	1150	0·239	0·42	2·70	2·68
Fractional crystallization at 1·0 GPa						
SV46	1·0	1330	1·000	0·10	2·82	2·82
SV44	1·0	1300	0·981	0·10	2·80	2·80
SV49	1·0	1270	0·884	0·11	2·79	2·80
SV53	1·0	1240	0·664	0·15	2·78	2·79
SV54	1·0	1210	0·453	0·22	2·78	2·78
SV57	1·0	1180	0·365	0·27	2·78	2·77
SV58	1·0	1150	0·175	0·57	2·75	2·72
SV61	1·0	1120	0·087	1·15	2·70	2·61
SV63	1·0	1090	0·068	1·47	2·68	2·57
SV64	1·0	1060	0·037	2·67	2·64	2·45
Equilibrium crystallization at 1·0 GPa						
SV12	1·0	1300	1·000	0·10	2·81	2·82
SV11	1·0	1270	0·975	0·10	2·80	2·81
SV13	1·0	1240	0·941	0·11	2·82	2·82
SV15	1·0	1210	0·726	0·14	2·82	2·82
SV27	1·0	1180	0·585	0·17	2·79	2·79
SV28	1·0	1150	0·527	0·19	2·79	2·79
SV25	1·0	1120	0·428	0·23	2·78	2·77
SV24	1·0	1090	0·311	0·32	2·76	2·75

Densities were calculated following the method of Lange & Carmichael (1987) and Lange (1994) for anhydrous (ρ_{dry}) conditions and with theoretical H$_2$O contents (ρ_{wet}) starting with 0·1 wt% for the primary liquid (HK19.1, 19.2). Water contents have been calculated treating H$_2$O as a totally incompatible element using the accumulated experimental melt fractions (MF$_{acc}$).

have low densities (and relatively low viscosities) that allow extraction from their solid residues and emplacement at shallow crustal levels, where they form either granitoid batholiths or large, ignimbrite-dominated volcanic complexes, both typical of magmatism associated with extensional tectonic settings, such as the Basin an Range Province of the Western USA or the Ivrea–Verbano–Serie dei Laghi complex in the Southern Alps of Northern Italy, where an entire cross-section from deep crustal (35 km depth) ultramafic–mafic cumulates to shallow-level (5–10 km depth) granitic intrusive rocks is exposed.

REFERENCES

Akella, J. & Boyd, F. R. (1972). Partitioning of Ti and Al between pyroxenes, garnets, and oxides. *Carnegie Institution of Washington Yearbook* **71**, 378–384.

Asimow, P. D. & Ghiorso, M. S. (1998). Algorithmic modifications extending MELTS to calculate subsolidus phase relations. *American Mineralogist* **83**, 1127–1131.

Baker, D. R. & Eggler, D. H. (1983). Fractionation paths of Atka (Aleutians) high alumina basalts: constraints from phase relations. *Journal of Volcanology and Geothermal Research* **18**, 387–404.

Baker, D. R. & Eggler, D. H. (1987). Compositions of anhydrous and hydrous melts coexisting with plagioclase, augite, and olivine or low-Ca pyroxene from 1 atm to 8 kbar: application to Aleutian volcanic center of Atka. *American Mineralogist* **72**, 12–28.

Baker, M. B., Grove, T. L. & Price, R. (1994). Primitive basalts and andesites from the Mt. Shasta region, N. California: products of varying melt fractions and water contents. *Contributions to Mineralogy and Petrology* **118**, 111–129.

Bartels, K. S., Kinzler, R. J. & Grove, T. L. (1991). High-pressure phase relations of primitive high-alumina basalts from Medicine Lake volcano, northern California. *Contributions to Mineralogy and Petrology* **108**, 253–270.

Bender, J. F., Hodges, F. N. & Bence, A. E. (1978). Petrogenesis of basalts from the project FAMOUS area: experimental study from 0 to 15 kbar. *Earth and Planetary Science Letters* **41**, 277–302.

Bergantz, G. W. (1989). Underplating and partial melting; implications for melt generation and extraction. *Science* **245**, 1093–1095.

Berndt, J., Koepke, J. & Holtz, F. (2005). An experimental investigation of the influence of water and oxygen fugacity on differentiation of MORB at 200 MPa. *Journal of Petrology* **46**, 135–167.

Bianchi, A., Callegari, E. & Jobstraibizer, P. G. (1970). I tipi petrografici fondamentali del Plutone dell'Adamello. *Memorie degli Istituti di Geologia e Mineralogia dell'Universita di Padova* **27**, 1–146.

Blundy, J. D., Falloon, T. J., Wood, B. J. & Dalton, J. A. (1995). Sodium partitioning between clinopyroxene and silicate melts. *Journal of Geophysical Research* **100**, 501–515.

Bohlen, S. R., Essene, E. J. & Boettcher, A. J. (1980). Reinvestigations and applications of olivine–quartz–orthopyroxene barometry. *Earth and Planetary Science Letters* **47**, 1–10.

Bose, K. & Ganguly, J. (1995). Quartz–coesite revisited: reversed experimental determinations at 500–1000°C and retrieved thermochemical properties. *American Mineralogist* **80**, 231–238.

Boyd, F. R. & England, J. L. (1960). Apparatus for phase-equilibrium measurements at pressures up to 50 kilobars and temperatures up to 1750°C. *Journal of Geophysical Research* **65**, 741–748.

Brey, G. P., Weber, R. & Nickel, K. G. (1990). Calibration of belt apparatus to 1800°C and 6 GPa. *Journal of Geophysical Research* **95**, 15603–15610.

Burnham, C. W. (1971). Water and magmas: a mixing model. *Geochimica et Cosmochimica Acta* **39**, 1077–1084.

Clark, S. P. (1959). Effect of pressure on the melting points of eight alkali halides. *Journal of Chemical Physics* **31**, 1526–1531.

Cox, K. G. (1980). A model for flood basalt volcanism. *Journal of Petrology* **21**, 629–650.

Demarchi, G., Quick, J. E., Sinigoi, S. & Mayer, A. (1998). Pressure gradient and original orientation of a lower-crustal intrusion in the Ivrea–Verbano Zone, Northern Italy. *Journal of Geology* **106**, 609–622.

Eggins, S. M. (1992). Petrogenesis of Hawaiian tholeiites: 1, phase equilibria constraints. *Contributions to Mineralogy and Petrology* **110**, 387–397.

Elthon, D. & Scarfe, C. M. (1984). High-pressure phase equilibria of a high-magnesia basalt and the genesis of primary oceanic basalts. *American Mineralogist* **69**, 1–15.

Forsythe, L. M., Nielsen, R. L. & Fisk, M. R. (1994). High-field-strength element partitioning between pyroxene and basaltic to dacitic magmas. *Chemical Geology* **117**, 107–125.

Fram, M. S. & Longhi, J. (1992). Phase equilibria of dikes associated with Proterozoic anorthosite complexes. *American Mineralogist* **77**, 605–616.

Frost, D. J. & Wood, B. J. (1995). Experimental measurements of the graphite C–O equilibrium and CO$_2$ fugacities at high temperatures and pressure. *Contributions to Mineralogy and Petrology* **121**, 303–308.

Gaetani, G. A. & Grove, T. L. (1998). The influence of water on melting of mantle peridotite. *Contributions to Mineralogy and Petrology* **131**, 323–346.

Ghiorso, M. S. & Carmichael, I. S. E. (1985). Chemical mass transfer in magmatic processes. II. Applications in equilibrium crystallization, fractionation and assimilation. *Contributions to Mineralogy and Petrology* **90**, 121–141.

Ghiorso, M. S. & Sack, R. O. (1995). Chemical mass transfer in magmatic processes IV. A revised and internally consistent thermodynamic model for the interpretation and extrapolation of liquid–solid equilibria in magmatic systems at elevated temperatures and pressures. *Contributions to Mineralogy and Petrology* **119**, 197–212.

Ghiorso, M. S., Hirschmann, M. M., Reiners, P. W. & Kress, V. C. I. (2002). The pMELTS: a revision of MELTS aimed at improving calculation of phase relations and major element partitioning involved in partial melting of the mantle at pressures up to 3 GPa. *Geochemistry, Geophysics, Geosystems* **3**, doi:10.1029/2001GC000217.

Green, D. H. & Ringwood, A. E. (1967). The genesis of basaltic magmas. *Contributions to Mineralogy and Petrology* **15**, 103–190.

Grove, T. L. & Baker, M. B. (1983). Effects of melt density on magma mixing in calc-alkaline series lavas. *Nature* **305**, 416–418.

Grove, T. L. & Baker, M. B. (1984). Phase equilibrium controls on the tholeiitic versus calc-alkaline differentiation trends. *Journal of Geophysical Research* **89**, 3253–3274.

Grove, T. L. & Bryan, W. B. (1983). Fractionation of pyroxene-phyric MORB at low pressure: an experimental study. *Contributions to Mineralogy and Petrology* **84**, 293–309.

Grove, T. L., Kinzler, R. J. & Bryan, W. B. (1990). Natural and experimental phase relations of lavas from Serocki Volcano. In: Detrick, R., Honnorez, J., Brian, W. B. *et al.* (eds) *Proceedings of the Ocean Drilling Program, Scientific Results, 106*. College Station, TX: Ocean Drilling Program, pp. 9–17.

Grove, T. L., Kinzler, R. J. & Bryan, W. B. (1992). Fractionation of mid-ocean ridge basalt (MORB). In: Phipps Morgan, J., Blackman, D. K. & Sinton, J. M. (eds) *Mantle Flow and Melt Generation at Mid-ocean Ridges. Geophysical Monograph, American Geophysical Union* **71**, 281–310.

Gust, D. A. & Perfit, M. R. (1987). Phase relations of a high-Mg basalt from the Aleutian Island Arc: implications for primary island arc basalts and high Al basalts. *Contributions to Mineralogy and Petrology* **97**, 7–18.

Hacker, B. R. & Abers, G. A. (2004). Subduction factory 3: an Excel worksheet and macro for calculating the densities, seismic wave speeds, and H$_2$O contents of minerals and rocks at pressure and temperature. *Geochemistry, Geophysics, Geosystems* **5**, doi: 10.1029/2003GC000614.

Hermann, J., Müntener, O. & Günther, D. (2001). Differentiation of mafic magma in a continental crust-to-mantle transition zone. *Journal of Petrology* **42**, 189–206.

Herzberg, C. (2004). Partial crystallization of mid-ocean ridge basalts in the crust and mantle. *Journal of Petrology* **45**, 2389–2405.

Herzberg, C. T., Fyfe, W. S. & Carr, M. J. (1983). Density constraints on the formation of the continental Moho and crust. *Contributions to Mineralogy and Petrology* **84**, 1–5.

Hill, E., Wood, B. J. & Blundy, J. D. (2000). The effect of Ca-Tschermaks component on trace element partitioning between clinopyroxene and silicate melt. *Lithos* **53**, 203–215.

Hirose, K. & Kushiro, I. (1993). Partial melting of dry peridotites at high pressures: determination of compositions of melts segregated from peridotite using aggregates of diamond. *Earth and Planetary Science Letters* **114**, 477–489.

Holbrook, W. S. & Kelemen, P. (1993). Large igneous province on the US Atlantic margin and implications for magmatism during continental break up. *Nature* **364**, 433–436.

Johnson, K. T. M. (1998). Experimental determination of partitioning coefficients for rare earth and high-field-strength elements between clinopyroxene, garnet, and basaltic melt at high pressures. *Contributions to Mineralogy and Petrology* **133**, 60–68.

Kägi, R. (2000). The liquid line of descent of hydrous, primary, calc-alkaline magmas and elevated pressure. An experimental approach. PhD Dissertation, ETH Zurich, 115 pp.

Kelemen, P. & Aharonov, E. (1998). Periodic formation of magma fractures and generation of layered gabbros in the lower crust beneath oceanic spreading ridges. In: Buck, W. R., Delaney, P. T., Karson, J. A. & Lagabrielle, Y. (eds) *Faulting and Magmatism at Mid-ocean Ridges. Geophysical Monograph, American Geophysical Union* **106**, 267–289.

Kelemen, P., Johnson, K. T. M., Kinzler, R. J. & Irving, A. J. (1990). High-field-strength element depletions in arc basalts due to mantle–magma interaction. *Nature* **345**, 521–524.

Kinzler, R. J. & Grove, T. L. (1992). Primary magmas of mid-ocean ridge basalts 1. Experiments and methods. *Journal of Geophysical Research* **97**, 6885–6906.

Kress, V. C. & Carmichael, I. S. E. (1991). The compressibility of silicate liquids containing Fe_2O_3 and the effect of composition, temperature, oxygen fugacity and pressure on their redox state. *Contributions to Mineralogy and Petrology* **108**, 82–92.

Kushiro, I. & Mysen, B. O. (2002). A possible effect of melt structure on the $Mg–Fe^{2+}$ partitioning between olivine and melt. *Geochimica et Cosmochimica Acta* **66**, 2267–2272.

Lange, R.A. (1994). The effect of H_2O, CO_2 and F on the density and viscosity of silicate melts. In: Carroll, M. R. & Holloway, J. R. (eds) *Volatiles in Magmas. Mineralogical Society of America, Reviews in Mineralogy* **30**, 331–369.

Lange, R.A. & Carmichael, I.S.E. (1987). Densities of $Na_2O–K_2O–CaO–MgO–FeO–Fe_2O_3–Al_2O_3–TiO_2–SiO_2$ liquids: new measurements and derived partial molar properties. *Geochimica et Cosmochimica Acta* **51**, 2931–2946.

Lightfoot, P. C., Hawkesworth, C. J., Devey, C. W., Rogers, N. W. & Van Calsteren, P. W. C. (1990). Source and differentiation of Deccan Trap lavas; implications of geochemical and mineral chemical variations. *Journal of Petrology* **31**, 1165–1200.

Lundstrom, C. C., Shaw, H. F., Ryerson, F. J., Williams, Q. & Gill, J. (1998). Crystal chemical control of clinopyroxene–melt partitioning in the Di–Ab–An system: implications for elemental fractionations in the depleted mantle. *Geochimica et Cosmochimica Acta* **62**, 2849–2862.

Michael, P. J. & Cornell, W. C. (1998). Influence of spreading rate and magma supply on crystallization and assimilation beneath mid-ocean ridges: evidence from chlorine and major element chemistry of mid-ocean ridge basalts. *Journal of Geophysical Research* **103**, 18325–18356.

Muan, A. (1958). Phase equilibria at high temperatures in oxide systems involving changes in oxidation states. *American Journal of Science* **256**, 171–207.

Müntener, O., Hermann, J. & Trommsdorff, V. (2000). Cooling history and exhumation of lower-crustal granulite and upper mantle (Malenco, Eastern Central Alps). *Journal of Petrology* **41**, 175–200.

Mutter, J. C., Talwani, M. & Stoffa, P. L. (1984). Evidence for a thick oceanic crust adjacent to the Norwegian margin. *Journal of Geophysical Research* **89**, 483–502.

Onuma, K. & Yagi, K. (1971). The join $CaMgSi_2O_6–Ca_2MgSi_2O_7–CaTiAl_2O_6$ in the system $CaO–MgO–Al_2O_3–TiO_2–SiO_2$ and its bearing on titan pyroxenes. *Mineralogical Magazine and Journal of the Mineralogical Society* **38**, 471–480.

Panjasawatwong, Y., Danyushevsky, L. V., Crawford, A. J. & Harris, K. L. (1995). An experimental study of the effects of melt composition on plagioclase–melt equilibria at 5 and 10 kbar: implications for the origin of magmatic high-An plagioclase. *Contributions to Mineralogy and Petrology* **118**, 320–432.

Pertermann, M. & Hirschmann, M. M. (2003). Anhydrous partial melting experiments on MORB-like eclogite: phase relations, phase compositions and mineral–melt partitioning of major elements at 2–3 GPa. *Journal of Petrology* **44**, 2173–2201.

Putirka, K., Johnson, M., Kinzler, R. J., Longhi, J. & Walker, D. (1996). Thermobarometry of mafic igneous rocks based on clinopyroxene–liquid equilibria, 0–30 kbar. *Contributions to Mineralogy and Petrology* **123**, 92–108.

Rivalenti, G., Garuti, G. & Rossi, A. (1975). The origin of the Ivrea–Verbano basic formation (western Italian Alps); whole rock geochemistry. *Bollettino della Società Geologica Italiana* **94**, 1149–1186.

Rivalenti, G., Rossi, A., Franca, S. & Sinigoi, S. (1984). The layered series of the Ivrea–Verbano igneous complex, Western Alps, Italy. *Tschermaks Mineralogische und Petrographische Mitteilungen* **33**, 77–99.

Roedder, P. L. & Emslie, R. F. (1970). Olivine–liquid equilibrium. *Contributions to Mineralogy and Petrology* **29**, 275–289.

Sano, T., Fujii, T., Deshnukh, S. S., Fukuoka, T. & Aramaki, S. (2001). Differentiation processes of Deccan Trap basalts: contribution from geochemistry and experimental petrology. *Journal of Petrology* **42**, 2175–2195.

Schmid, R. & Wood, B. J. (1976). Phase relationships in granulitic metapelites from the Ivrea–Verbano Zone (Northern Italy). *Contributions to Mineralogy and Petrology* **54**, 255–279.

Sisson, T. W. & Grove, T. L. (1993). Experimental investigations of the role of H_2O in calc-alkaline differentiation and subduction zone magmatism. *Contributions to Mineralogy and Petrology* **113**, 143–166.

Sparks, R. S. I., Meyer, P. & Sigurdsson, H. (1980). Density variation amongst mid-ocean ridge basalts: implications for magma mixing and the scarcity of primitive lavas. *Earth and Planetary Science Letters* **46**, 419–430.

Stolper, E. & Walker, D. (1980). Melt density and the average composition of basalt. *Contributions to Mineralogy and Petrology* **74**, 7–12.

Thompson, R. N. (1974). Some high-pressure pyroxenes. *Mineralogical Magazine* **39**, 768–787.

Thompson, R. N., Gibson, I. L., Marriner, G. F., Mattey, D. P. & Morrison, M. A. (1980). Trace-element evidence of multistage mantle fusion and polybaric fractional crystallisation in the Paleocene lavas of Skye, NW Scotland. *Journal of Petrology* **21**, 265–293.

Thy, P., Lesher, C. E. & Mayfield, J. D. (1999). Low-pressure melting studies of basalt and basaltic andesite from the southeast Greenland continental margin and the origin of dacites at site 917. In: Larsen, H. C., Duncan, R. A., Allan, J. F., Brooks, K. *et al.* (eds) *Proceedings of the Ocean Drilling Program, Scientific Results, 163.* College Station, TX: Ocean Drilling Program, pp. 95–112.

Toplis, M. J., Libourel, G. & Carroll, M. R. (1994). The role of phosphorus in the crystallisation processes of basalt: an experimental study. *Geochimica et Cosmochimica Acta* **58**, 797–810.

Tormey, D. R., Grove, T. L. & Bryan, W. B. (1987). Experimental petrology of normal MORB near the Kane Fracture Zone: 22–25°N, mid-Atlantic ridge. *Contributions to Mineralogy and Petrology* **96**, 121–139.

Ulmer, P. (1989). The dependence of the $Fe^{2+}–Mg$ cation-partitioning between olivine and basaltic liquid on pressure, temperature and composition. An experimental study to 30 kbars. *Contributions to Mineralogy and Petrology* **101**, 261–273.

Ulmer, P. & Luth, R. W. (1991). The graphite–COH fluid equilibrium in P, T, fO_2 space. An experimental determination to 30 kbar and 1600°C. *Contributions to Mineralogy and Petrology* **106**, 265–272.

Verhoogen, J. (1962). Distribution of titanium between silicates and oxides in igneous rocks. *American Journal of Science* **260**, 211–220.

Villiger, S., Ulmer, P., Müntener, O. & Thompson, A. B. (2004). The liquid line of descent of anhydrous, mantle-derived, tholeiitic liquids by fractional and equilibrium crystallization—an experimental study at 1·0 GPa. *Journal of Petrology* **45**, 2369–2388.

Villiger, S., Müntener, O. & Ulmer, P. (2006). Crystallization pressures of mid-ocean ridge basalts derived from major element variations of glasses from equilibrium and fractional crystallization experiments. *Journal of Geophysical Research, Solid Earth*, doi: 10.1029/2006JB004342 (in press).

Wood, B. J. & Trigila, R. (2001). Experimental determination of aluminous clinopyroxene–melt partition coefficients for potassic liquids, with application to the evolution of the Roman province potassic magmas. *Chemical Geology* **172**, 213–223.

Yang, H. J., Kinzler, R. J. & Grove, T. L. (1996). Experiments and models of anhydrous, basaltic olivine–plagioclase–augite saturated melts from 0·001 to 10 kbar. *Contributions to Mineralogy and Petrology* **124**, 1–18.